



# On the link between fracture toughness, tensile strength, and fracture process zone in anisotropic rocks

**Journal Article****Author(s):**

[Dutler, Nathan](#) ; Nejadi, Morteza; Valley, Benoît; Amann, Florian; [Molinari, Giulio](#) 

**Publication date:**

2018-10-01

**Permanent link:**

<https://doi.org/10.3929/ethz-b-000288627>

**Rights / license:**

[Creative Commons Attribution-NonCommercial-NoDerivatives 4.0 International](#)

**Originally published in:**

Engineering Fracture Mechanics 201, <https://doi.org/10.1016/j.engfracmech.2018.08.017>

**Funding acknowledgement:**

150729 - Optical measurement of three-dimensional surface displacement fields of morphing structures (SNF)

# On the link between fracture toughness, tensile strength, and fracture process zone in anisotropic rocks

Nathan Dutler<sup>a</sup>, Morteza Nejati<sup>\*b</sup>, Benoît Valley<sup>a</sup>, Florian Amann<sup>c</sup>, Giulio Molinari<sup>d</sup>

<sup>a</sup>Center for Hydrogeology and Geothermics, University of Neuchâtel, Neuchâtel, Switzerland

<sup>b</sup>Department of Earth Sciences, ETH Zurich, Switzerland

<sup>c</sup>Chair of Engineering Geology and Environmental Management, RWTH Aachen, Germany

<sup>d</sup>Laboratory of Composite Materials and Adaptive Structures, Department of Mechanical and Process engineering, ETH Zurich, Switzerland

---

## Abstract

This paper presents experimental results on the anisotropy of the fracture toughness, Brazilian tensile strength, and the fracture process zone (FPZ) in granodiorite samples. The fracture toughness is measured using semi-circular bending tests, while Brazilian disk tests were conducted to measure the tensile strength indirectly. Digital image correlation (DIC) was employed to obtain full-field surface deformation associated with the fracture propagation and identify the FPZ. An averaging scheme is proposed to determine the length and width of the FPZ from the strain field. The DIC results confirm a semi-elliptical FPZ developing ahead of the crack tip, with an average length-to-width ratio of approximately two. The results also indicate that the theoretical models such as Irwin and strip-yield with uniform traction, which are based on plastic deformation near the crack tip, underestimate the extent of the inelastic zone, while the strip-yield model with a linear cohesion stress distribution overestimate the length of the process zone. The anisotropy ratio of the FPZ length obtained from the models, however, agrees very well with the ratio obtained from the DIC measurements. This evidence supports the basis of the theoretical models that predict the FPZ length to be proportional to the square of fracture toughness over tensile strength.

*Keywords:* Fracture toughness anisotropy, Strength anisotropy, Fracture process zone, Digital image correlation, Transverse isotropy.

---

## 1. Introduction

The mechanics of crack growth in rocks is an important field of research with direct applications in many geoscience and geoengineering fields including geothermal energy production, min-

---

*Email address:* \*mnejati@ethz.ch (Morteza Nejati\*)

### Nomenclature

$\alpha$	Dimensionless crack length
$a$	Initial crack length
$B$	Specimen thickness
$D$	SCB and BD diameter
$E, E'$	Young's moduli within and normal to the isotropy plane
$\epsilon_{ij}$	Strain component $ij$
$\epsilon_1$	Maximum principal strain
$\phi$	Angle between the crack plane and the foliation (isotropy) plane
$G, G'$	Shear moduli within and normal to the plane of isotropy
$L$	FPZ length
$K_I$	Mode I stress intensity factor
$K_{Ic}$	Mode I fracture toughness
$L_1^p, L_S^p$	Length of the plastic zone by the Irwin's and strip-yield models
$L_1$	Length of the process zone estimated from Irwin's model
$L_{Su}, L_{S1}, L_{Sn}$	Length of the process zone estimated from strip-yield model with uniform, linear and nonlinear cohesion stress variation along the FPZ
$\nu, \nu'$	Poisson's ratio within and normal to the plane of isotropy
$P, P_m$	Load and peak load
$R$	Sample radius
$r, \theta$	Polar coordinates of a point near the crack tip
$S$	Span length
$S_{ij}$	Compliance matrix component $ij$
$\sigma_t$	Tensile strength
$\sigma_t^{iso}$	Tensile strength calculated based on isotropic elasticity assumption
$\sigma_u$	Yield strength
$\sigma_i$	Normal stress component in $i$ direction
$\tau_{ij}$	Shear stress $ij$
$u, v$	Displacements along $x$ and $y$ directions
$\mu_i, \bar{\mu}_i$	Conjugate pair of roots to the 4th order characteristic equation of anisotropic elasticity $i = 1, 2$
$x, y$	Cartesian coordinates
$Y_I, Y_{II}$	Normalised stress intensity factors for modes I and II
$W$	FPZ width
<b>Abbreviations</b>	
AE	Acoustic emission
BD	Brazilian disk
CB	Chevron bend
CCNBD	Cracked chevron notched Brazilian disc
DIC	Digital image correlation
FPZ	Fracture process zone
GTS	Grimsel Test Site
ISRM	International Society for Rock Mechanics
LEFM	Linear elastic fracture mechanics
SCB	Semi-circular bend
SR	Short rod

ing, tunneling, earthquake seismology, and reservoir geomechanics. In order to analyse the mechanics of fracturing in rocks, mechanical properties such as elasticity constants, strength and fracture toughness have to be accurately measured. An example of the importance of the anisotropy in rock mass response to external loading was recently demonstrated in an in-situ stimulation and circulation project in the deep underground laboratory at the Grimsel Test Site in Switzerland (Amann et al., 2018; Gischig et al., 2018; Jalali et al., 2018). Elasticity parameters characterize the elastic deformation of rock due to the applied load, while strength is the critical tensile or compressive stress at which the rock fails. Closely related to the strength is a parameter called fracture toughness which is a measure of the resistance of rock against crack growth. Fracture toughness is a key intrinsic material property used in analyzing brittle fracture growth.

Due to the texture or layered structure developed during the formation or metamorphic process (e.g. foliation, bedding), a large class of rocks have anisotropic mechanical properties such as elasticity, strength and fracture toughness. The anisotropy of fracture toughness implies the directional-dependency of the rock resistance against crack growth. In the context of linear elastic fracture mechanics, the fracture toughness is closely related to the concept of the fracture energy  $G_f$  defined by Griffith. The Griffith theory of fracture growth postulates that the strain energy

20 released due to the fracture growth is consumed to create the fracture surfaces. The process of  
21 creating fracture surfaces may involve dissipation of energy by heat, wave propagation, inelastic  
22 deformation near the fracture surfaces and bonds breakage between the fracture surface (Olgaard  
23 and Brace, 1983; Hoagland et al., 1973).

24 The growth of crack in rocks is accompanied by significant inelastic deformation near the  
25 crack tip. This highly damaged region adjacent to the crack tip is called fracture process zone  
26 (FPZ) within which the material undergoes micro-damaging. In the fracture process zone, micro-  
27 cracks close or open depending on their orientation with respect to the direction of the applied  
28 load, and crack growth in fact occurs by connecting the micro-cracks at a critical load. The fracture  
29 toughness  $K_{Ic}$  gives the intensity of stress at this critical state. One of the reasons for the anisotropy  
30 of the fracture toughness and tensile strength is the preferential direction of pre-existing micro-  
31 cracks, which seems to be mostly aligned with the textural orientation of rock such as foliation or  
32 bedding. Therefore, the interaction of newly developed micro-cracks with the pre-existing ones,  
33 in terms of density, size and orientation, is central in understanding the anisotropy of the fracture  
34 toughness (Anders et al., 2014).

35 The anisotropic elasticity of foliated and sedimentary rocks can be efficiently modeled through  
36 a transversely isotropic constitutive behavior which includes five elastic constants in the model.  
37 This approximation relies on the fact that there is an isotropic plane normal to which a different  
38 Young's modulus is to be expected. The isotropy plane is often assumed to be the foliation or  
39 bedding plane of the rock. Apart from the elasticity, strength and toughness are also expected  
40 to be anisotropic and dependent on the direction of the applied load with respect to the plane  
41 of anisotropy. Most of the studies conducted on the anisotropy of fracture toughness focus on  
42 the anisotropic ratio and its correlation with the micro-crack structure of rock (see a review in  
43 Section 2). However, a key ingredient of fracturing is the fracture process zone (FPZ), and the  
44 development and characteristics of this zone in anisotropic rocks have not been investigated so  
45 far. Most of research on FPZ development is focused on concrete, and occasionally on some  
46 isotropic rocks. It is well known that the FPZ has a central role in linking the fracture toughness  
47 and strength.

48 This work investigates the anisotropy of the tensile strength and mode I fracture toughness  
49 in granodiorite samples from Grimsel Test Site (GTS) in Switzerland. Digital image correlation  
50 (DIC) is employed to observe the development of fracture process zone near the crack tip. An  
51 averaging method is used to calculate the width of the FPZ from strain and displacement fields.  
52 The size and shape of the FPZ calculated from the DIC results are then used to evaluate the  
53 anisotropy of the FPZ. The results show that the FPZ develops as a semi-elliptical localized region,

54 with the ratio of length to width being about two in both principal directions (isotropic shape).  
55 However, the actual values of the length and width show slight anisotropy, with the size of the  
56 FPZ being bigger for cracks oriented along the foliation compared to the ones oriented normal to  
57 the foliation plane. It is also shown that the theoretical models such as Irwin and strip-yield with  
58 uniform traction underestimate the extent of the inelastic zone, while the strip-yield model with a  
59 linear cohesion stress distribution overestimate the length of the process zone. However, the ratio  
60 of the FPZ lengths at principal directions fits the theoretical models very well. This indicates that  
61 the length of the FPZ is indeed proportional to the square of fracture toughness over strength.

## 62 **2. Fracture toughness and strength**

### 63 *2.1. Fracture toughness measurement*

64 Several methods of measuring mode I fracture toughness exist in literature. Reviews on various  
65 methods with their attributes, advantages and drawbacks are given in Whittaker et al. (1992) and  
66 Bearman (1999). To obtain precise, accurate and consistent results, the International Society for  
67 Rock Mechanics (ISRM) recommends four test procedures: (1) Chevron bend (CB) (Ouchterlony,  
68 1988); (2) Short rod (SR) (Ouchterlony, 1988); (3) Cracked chevron notched Brazilian disc (CC-  
69 NBD) (Fowell, 1995); and (4) Notched semi-circular bend (SCB) (Kuruppu et al., 2014). These  
70 standards indicate the requirements for the samples in terms of their preparation, dimensions, and  
71 test procedure in terms of loading type and rate. Formulae are also provided to calculate the  
72 fracture toughness from the failure load and geometrical factors.

73 Despite standardized testing, the results from CB, SR and CCNBD exhibit a deviation in the  
74 range of 20-30%. This deviation is often explained by size effects, anisotropy of the rock and  
75 inaccuracy of the dimensionless parameters used in the calculation. Among these methods, the  
76 CCNBD show a consistently lower variation (Dwivedi et al., 2000). Iqbal and Mohanty (2007)  
77 compared CB and CCNBD methods on three different rock types with two-hundred specimens  
78 and concluded that the methods are very comparable when the correct equation for fracture tough-  
79 ness calculation was used and the specimen size was selected carefully. Kataoka et al. (2015b)  
80 compared CB and SCB method using Kimachi sandstone and obtained almost the same values. In  
81 term of size effects, the recommended ISRM procedure for a specific method allows to minimize  
82 the variation of fracture toughness values among the different methods.

83 The effect of rock anisotropy on fracture toughness has been investigated in a number of stud-  
84 ies. Krishnan et al. (1998) and Ke et al. (2008) studied the fracture toughness anisotropy of sand-  
85 stone and marble using Cracked Straight Through Brazilian Disc (CSTBD) specimens. Kataoka  
86 and Obara (2012) and Kataoka et al. (2015a) used the SCB method to study two end-member

Table 1: A summary of findings on the fracture toughness of anisotropic rocks

Rock type	Methodology	Important Results	Reference
Sandstone Marble	Notched Brazilian disk specimen Microscopic analysis Mixed mode I/II experiments	<ul style="list-style-type: none"> <li>• Mixed-mode I/II fracture envelopes were developed.</li> <li>• The effect of anisotropy on fracture toughness can be significant.</li> </ul>	Krishnan et al. (1998); Ke et al. (2008)
Granite	Cracked chevron notched Brazilian disk specimen Microscopic analysis Acoustic Emission 3D X-ray and CT scans	<ul style="list-style-type: none"> <li>• Micro-crack density and length are major contributors to the value of fracture toughness.</li> <li>• Fracture toughness is inversely proportional to micro-crack density and length.</li> <li>• There is a correlation between fracture toughness and fracture roughness.</li> <li>• FPZ from acoustic emission and optical measurement are in good agreement.</li> <li>• The seismic velocities is closely linked to the micro-crack density and its orientation.</li> <li>• A decreasing anisotropy was observed with the increase of the loading rate.</li> </ul>	Nasseri et al. (2005, 2006); Nasseri and Mohanty (2008); Nasseri et al. (2009, 2010, 2011); Dai et al. (2013)
Granite	Notched semi-circular bend specimen Acoustic emission Ultrasonic measurements Microscopic analysis 3D X-ray CT scans	<ul style="list-style-type: none"> <li>• Orientation of micro-cracks can be estimated by measurement of wave velocity.</li> <li>• Both elastic wave velocity and fracture toughness exhibit anisotropy.</li> <li>• Fracture toughness is dependent on the micro-structure of rock.</li> <li>• <math>K_{Ic}</math> decreases with increasing water vapor pressure.</li> </ul>	Kataoka et al. (2015a)
Shale	Notched semi-circular bend specimen Microscopic analysis	<ul style="list-style-type: none"> <li>• The influence of calcite-filled veins on propagation path is investigated.</li> <li>• The propagation is strongly influenced by the approach angle of the induced fracture to the veins and the thickness of the veins.</li> </ul>	Lee et al. (2015)
Shale	Short rod specimen Ultrasonic measurements Microscopic analysis	<ul style="list-style-type: none"> <li>• Strong fracture toughness anisotropy was observed in shale.</li> <li>• <math>K_{Ic}</math> changes very little up to 120° at which temperature it starts to increase slightly.</li> <li>• When the original crack is oriented normal to the bedding, there is a strong tendency to deviate towards the bedding.</li> </ul>	Chandler et al. (2016, 2017)

87 configurations (named as short-transvers and arrester) of anisotropy in rocks under water-vapor  
88 pressure. The CCNBD method was used by Nasseri and Mohanty (2008) to measure the frac-  
89 ture toughness of different granitic rocks and sandstones at different orientations. Chandler et al.  
90 (2016) and Chandler et al. (2017) used a SR method to study Mancos shale in three configurations  
91 arrester, divider and short-transverse, at different temperatures. The SCB method was used by  
92 Funatsu et al. (2012) to study the relationship between fracture toughness and loading axis with  
93 respect to the bedding planes using sandstone.

94 In this study, the notched semi-circular bend configuration is used for investigating the fracture  
95 toughness anisotropy in Grimsel Granodiorite. The advantages of using SCB specimens are (1)  
96 it requires small samples, (2) sample preparation is easy due to minimal machining, and (3) only  
97 the failure load is required to determine the fracture toughness (Kuruppu et al., 2014). The effect  
98 of anisotropy can also be studied in a straightforward fashion by using SCB samples. Using this  
99 method, it is necessary to use slow loading rates so that the dynamic effects can be ignored.

## 100 2.2. Anisotropy of fracture toughness

101 Table 1 summarizes the findings on the anisotropic fracture toughness in different types of  
102 rocks. An important result is the identification of the central role of micro-structure orientation and  
103 grain size in the anisotropy of the fracture toughness. The fracture toughness is closely linked to  
104 the presence of micro-cracks and their orientation. It is in fact reported that micro-crack structure  
105 in crystalline rock is more important than the grain size and orientation when it comes to the  
106 fracture toughness (Nasseri and Mohanty, 2008).

107 A correlation between the orientation of foliation/bedding and the maximum of P-wave veloc-  
108 ity was observed in granite and shale (Nasseri and Mohanty, 2008; Chandler et al., 2016). The  
109 highest P-wave velocity is measured parallel to foliation/bedding while the minimum value was

110 obtained in the direction normal to the foliation/bedding. This fact indicates that the micro-cracks  
111 are dominantly oriented along the foliation/bedding. The reason for lower measured values of  
112 fracture toughness along foliation and bedding seems to be the higher density of micro-cracks in  
113 those directions. The process of fracture growth is explained by the gradual initiation and growth  
114 of (existing) micro-cracks, and their coalescence to form larger cracks. Therefore, higher density  
115 and larger micro-cracks facilitates the growth of fracture in certain directions.

116 The presence of a correlation between fracture toughness and fracture surface roughness of  
117 Stanstead and Barre granite was suggested by Nasser et al. (2009, 2010). Their study shows  
118 a significant increase of  $K_{Ic}$  and fracture roughness between directions parallel to and normal to  
119 petrofabric orientation. In addition, the rock with a coarser micro-structural fabric shows a rougher  
120 fracture surface. The results generally confirm an essential link among petrofabric anisotropy, frac-  
121 ture toughness, fracture roughness, and evolution and extent of associated induced cracks along  
122 specific directions in the fracture process zone. Similar results have been shown for shale, where  
123 the fracture growing normal to the direction of bedding seems to be tortuous and kinked, inducing  
124 a rougher fracture surface (Chandler et al., 2016).

### 125 *2.3. Anisotropy of strength*

126 The tensile strength of brittle materials can be obtained by direct or indirect methods. A simple  
127 indirect method is the Brazilian tensile test in which a thin circular disk is loaded diametrically up  
128 to failure (see reviews by Li and Wong (2013) and Perras and Diederichs (2014)). This diametrical  
129 compression induces a tensile stress normal to the direction of applied load, and it is expected that  
130 the specimen failure initiates at the point of maximum tensile stress, i.e. at the center of disk.  
131 The elasticity solution that calculates the stress at the center of disk is based on a homogeneous,  
132 isotropic and linearly elastic material behavior (Hondros, 1959; Bieniawski and Bernede, 1979;  
133 ASTM, 2008), and requires only the peak load and sample dimensions to calculate the tensile  
134 strength. With the introduction of anisotropic elasticity, the solution is not only a function of  
135 loading and geometry dimensions, but also the elastic constants of the anisotropic material. The  
136 explicit representation of stress in a Brazilian disk with transversely isotropic material has been  
137 given by Chen et al. (1998); Exadaktylos and Kaklis (2001) and Claesson and Bohloli (2002).  
138 These studies are based on the Lekhnitskiy's anisotropic elasticity solution (Lekhnitskiy, 1969),  
139 and show that the elasticity solution of Brazilian disk depends on two material parameters.

140 The early work of Barla and Innaurato (1973) investigated the suitability of Brazilian and ring  
141 tests for the measurement of tensile strength. Using finite element simulations, they concluded that  
142 the anisotropy has a significant influence on the stress at the center of disk, and therefore the tensile  
143 strength measurement based on an isotropic elasticity solution may be significantly inaccurate.

144 They also found that the failure may occur along the bedding or foliation, and not always along the  
145 loading direction, which raises serious doubts on the nature of failure process. Many experimental  
146 results on anisotropic rocks show that the micro-structure orientation can significantly influence  
147 the strength of rock, with the strength along the bedding or foliation is significantly lower than  
148 perpendicular to it (Tavallali and Vervoort, 2010; Vervoort et al., 2014; Khanlari et al., 2015; Wild  
149 et al., 2015). It has also been shown that when the foliation or bedding is oblique to the direction  
150 of applied load, a significant shearing component develops at the plane of failure, which raises  
151 doubts on the suitability of the results to be considered as tensile strength.

### 152 **3. Fracture process zone**

153 This section provides a review on the previous work related to the development of the FPZ in  
154 quasi-brittle materials.

#### 155 *3.1. Characteristics of process zone*

156 Linear elastic fracture mechanics describe a square-root singular stress state adjacent to the tip  
157 of a sharp crack. However, no material is able to resist an infinite amount of stress, and therefore  
158 the material undergoes an inelastic deformation in the vicinity of the crack tip. This inelastic  
159 region is of different nature depending on the material type. Metals often exhibit yielding and  
160 plasticity, often accompanied with strain hardening, due to the distortional component of stress.  
161 For this reason, the inelastic region near the tip in metals is called the plastic zone. On the other  
162 hand, brittle materials often exhibit damage due to initiation and propagation of micro-cracks,  
163 which is accompanied with strain softening and mainly driven by normal components of stress.  
164 For this reason, the inelastic region in brittle materials is often called fracture process zone (FPZ).  
165 In materials such as rock and concrete, the size of the FPZ can be large enough to introduce  
166 significant nonlinearity (softening) near the failure point. These materials derive their toughness  
167 from subcritical cracking that precedes the ultimate failure. This is the reason to name this types of  
168 materials as "quasi-brittle" rather than "brittle". Both plastic and fracture process zones are regions  
169 where considerable energy dissipation occurs. The fracture energy and toughness will therefore  
170 depend on the strength of the degree of nonlinearity and the size and shape of these zones.

171 The FPZ develops as a transition zone between the macro-crack which has strong discontinuity  
172 and the remote region which is assumed to be continuous in micro-scale. In fact, the process of  
173 fracture growth is described by the transition of the material behavior in the FPZ from micro-  
174 scale continuum to micro-scale discontinuum due to initiation and propagation of micro-cracks.  
175 These micro-cracks inside the FPZ then coalesce to form a macro-scale discontinuity represented



176 as fracture surfaces. In other words, the FPZ acts as a bridging zone between cracked region  
177 and uncracked region. This transition process dissipates strain energy to create new micro-cracks  
178 and damage zones. Therefore, more efficient energy dissipation mechanisms in the FPZ, and  
179 bigger sizes of process zone lead to higher energy dissipation which can be regarded as higher  
180 resistance of the materials against failure and fracturing. This is the reason why the fracture  
181 energy is significantly influenced by the FPZ characteristics. The stages of the development of  
182 the micro-crack damage zone around a crack tip in rock have been described in Hoagland et al.  
183 (1973).

184 There have been mainly two models to estimate the size of plastic zone under mode I loading:  
185 The Irwin approach, and the strip-yield model. Irwin (1961) estimated the plastic zone size by  
186 equating the normal stress along crack plane to the yield stress. This first approximation was then  
187 improved by considering the stress redistribution along the crack plane, giving a simple formula  
188 of  $L_1^p = (K_I/\sigma_u)^2/\pi$ , where  $L_1^p$  is the size of plastic zone in the crack plane,  $K_I$  is the mode I stress  
189 intensity factor and  $\sigma_u$  is the yield strength. The strip-yield model was proposed independently by  
190 Barenblatt (1959) and Dugdale (1960), and considers the inelastic zone in front of the crack tip  
191 as a part of a larger crack extending to the end of inelastic zone and having a uniform cohesion  
192 stress equal to a yield strength applied on its boundary. The method uses superposition principle  
193 to give an approximation of inelastic zone which vanishes the stress singularity, and gives a simple  
194 approximation of  $L_S^p = \pi(K_I/\sigma_u)^2/8$ . Irwin and strip-yield models predicts close values for the  
195 size of the plastic zone for small values of  $K_I/\sigma_u$ . For brittle material, one can simply replace  
196 the yield strength  $\sigma_u$  by the tensile strength  $\sigma_t$  to estimate the size of the FPZ. The size of a fully  
197 developed FPZ on the onset of fracture propagation ( $K_I = K_{Ic}$ ) is given by  $L_I = (K_{Ic}/\sigma_t)^2/\pi$  and  
198  $L_{S_u} = \pi(K_{Ic}/\sigma_t)^2/8$  based on Irwin and strip-yield models. These estimations assume a uniform  
199 stress being applied along the length of the FPZ, and therefore they are not expected to give  
200 very accurate predictions of FPZ length since the inelastic deformation has the nature of micro-  
201 damaging rather than plasticity in quasi-brittle materials. Taking into account a linear reduction of  
202 traction with proximity to the tip, Labuz et al. (1985) modified the strip-yield model to adjust for  
203 the micro-damaging of the rock material in the FPZ. This approximation gives a longer FPZ length  
204 with the relation  $L_{S_t} = 9\pi(K_{Ic}/\sigma_t)^2/32$ . Since both  $K_{Ic}$  and  $\sigma_t$  are considered material properties,  
205 the size of the FPZ is also expected to be a material property.

206 Models describing the shape of the inelastic zone are based on determining the boundary of  
207 a region within which a component or invariant of elastic stress exceeds the yield stress. Unlike  
208 the metals in which a distortion-based criterion like Von Mises governs best the plastic behaviour,  
209 the nonlinear micro-crack zone in quasi-brittle materials is mainly developed due to the tensile

210 stress. The most well-known criterion to describe the shape and size of the FPZ is the maximum  
211 normal stress introduced by Schmidt (1980). According to this criterion, the FPZ is formed in  
212 the region where the local maximum principal stress exceeds the tensile strength of the material.  
213 This model uses the elastic stress field near the tip and solve for the boundary of the region where  
214 maximum principal stress reaches the strength. This model, however, does not account for the  
215 redistribution of stress outside the FPZ while inelastic deformation occurs inside the FPZ, and  
216 therefore underestimate the size of the FPZ. As will be explained later, most of the experiments  
217 suggest a band-shaped (semi-elliptical) process zone for quasi-brittle materials which does not  
218 match the butterfly shape suggested by Schmidt (1980). The main reason might be that the the  
219 Young's modulus reduces mainly in the direction normal to the fracture plane in the process zone,  
220 and the reduction of strength within the process zone due to micro-cracking may lead to elongation  
221 of the process zone. One therefore should account for the the reduction of elastic properties and  
222 strength, perhaps using an anisotropic damage model, in order to provide a better model for the  
223 shape of the FPZ in quasi-brittle materials.

224 The FPZ size and shape are expected to depend only on the loading mode of the crack and the  
225 material properties and not on the specimen configuration. However, this is only true when the  
226 material properties such as  $K_{Ic}$  and  $\sigma_t$  do not exhibit specimen size and configuration dependence.  
227 For example,  $K_{Ic}$  is dependent on the size of specimen for smaller specimens mainly for two  
228 reasons: (i) the LEFM theory is unable to give good approximation of stress field when the FPZ  
229 is large compared to the crack size, (ii) even if one still considers the LEFM theory for crack with  
230 large nonlinear zones, the FPZ is likely to develop outside the singular dominant region, where  
231 only singular terms of the crack elastic solution are not sufficient to characterise the stress field. In  
232 other words, when the FPZ is large enough compared to the size of the crack and crack ligaments,  
233 higher order terms of the elastic solution also play a role in stress characterisation near the crack  
234 tip, and influence the FPZ development (Smith et al., 2001; Aliha et al., 2010). This is why the  
235 FPZ is also specimen size dependent for small specimens. Experimental observations also indicate  
236 that the boundary of specimen can influence the size of the FPZ and prevent the FPZ to develop  
237 fully (Zietlow and Labuz, 1998). The significant size of the FPZ compared to the specimen size  
238 is the main reason for the size dependency of strength and fracture toughness. This is why the  
239 FPZ plays an important role in determining a characteristic length of the micro-structure that  
240 reflects size effects. The fracture energy is closely related to the FPZ size and this implies that the  
241 existence of a FPZ may be the intrinsic cause for size effects. The applicability of linear elastic  
242 fracture mechanics for analyzing cracked structures is therefore determined by how big the FPZ is  
243 compared to the size of the specimen.

### 244 3.2. Experimental methods to evaluate FPZ

245 The importance of the FPZ in understanding the size effect phenomenon in quasi-brittle ma-  
246 terials has encouraged many researchers to experimentally observe the development of the FPZ.  
247 The observation of fracture process zone is difficult because of the small scale at which micro-  
248 structural events occur. The experimental techniques used to determine the FPZ in quasi-brittle  
249 materials can be divided into three categories:

- 250 • **Visual and image-based** methods such as optical and photoelectron microscopy, moiré in-  
251 terferometry, and digital image correlation (DIC): These methods rely on the analysis of  
252 images obtained from the surfaces of cracked specimens. The region of inelastic deforma-  
253 tion is then identified by analyzing the changes in the surfaces due to highly localized strain  
254 near the tip of fractures (Chengyong et al., 1990; Guo et al., 1993). DIC has been particu-  
255 larly popular recently due to simplicity, availability and the fact that it can provide a very  
256 accurate full-field measurement of strain field (Wu et al., 2011; Lin and Labuz, 2013; Lin  
257 et al., 2014). The resolution of the full-field data obtained from the DIC is considerably  
258 high, often below  $1 \mu m$ .
- 259 • **Acoustic-based** methods such as acoustic emission and ultrasonic probing: These methods  
260 utilize the information obtained from active and passive seismic waves traveling within the  
261 cracked specimens. Acoustic emission analyses the micro-seismic events generated by the  
262 inelastic mechanisms like micro-cracking and traces the location of micro-seismic event (Zi-  
263 etlow and Labuz, 1998; Backers et al., 2005; Lin et al., 2009). Ultrasonic probing, on the  
264 other hand, analyses the attenuation of active ultrasonic waves when they travel through a  
265 region of high inelastic deformation (Swanson and Spetzler, 1984; Labuz et al., 1987; Zang  
266 and Wagner, 2000).
- 267 • **Mechanical property-based** methods such as microhardness and nanoindentation: These  
268 methods are based on using nano- or micro-indentors to perform small scale load tests  
269 around the tip of cracks. A change in hardness is expected inside the FPZ since the material  
270 has undergone inelastic deformation. The boundary of the FPZ can then simply identified  
271 based on the change in hardness. Plastic deformation in metals is often accompanied with  
272 an increase in nanomechanical properties whereas damaged zones in quasi-brittle materials  
273 have a reduction in nanomechanical properties (Brooks et al., 2012, 2013; Brooks, 2013).

274 A noteworthy review of the works done using most of these techniques is given in Brooks  
275 et al. (2013). Among methods mentioned above, the AE and DIC seem to have attracted a lot of

276 attention. The ability of AE to trace the inelastic deformation not only on the surface but also  
277 inside the cracked specimens has made this method very powerful for characterising the FPZ.  
278 The main drawback of this method is high possible errors in determining the events' locations  
279 due to the uncertainty in the velocity model. Alam et al. (2014, 2015) used both the AE and DIC  
280 simultaneously and concluded that material damaging can change the velocity model significantly,  
281 and the location inaccuracy in their experiments is in the range of 5 mm. Therefore, an accurate  
282 determination of the FPZ size can be difficult to achieve with the AE. The DIC, on the other  
283 hand, provides very accurate full-field displacement and strain measurement on the surfaces of  
284 the cracked specimens. When performed using high-speed camera, the DIC is able to trace the  
285 mechanisms of fracture growth at the peak load very accurately.

### 286 3.3. *Lessons learned from past experiments*

287 On the basis of the results obtained from different experimental techniques used to characterise  
288 the FPZ in quasi-brittle materials, we can summarize the current knowledge as following:

- 289 1. There is a general consensus among the researchers that a positive correlation exists between  
290 the grain size (aggregate size in concrete) and the width of the FPZ. This means that the  
291 larger the grain size, the bigger the FPZ width in quasi-brittle materials (Chengyong et al.,  
292 1990; Otsuka and Date, 2000; Brooks et al., 2012; Brooks, 2013; Skarżyński and Tejchman,  
293 2013). Zietlow and Labuz (1998) measured the width of the FPZ for four different rock types  
294 and suggested that there exists a linear relation between the FPZ width and the logarithm  
295 of the grain size. The reason for this trend is perhaps due to a relation between the grain  
296 size and micro-crack density. Finer grained materials develop more micro-cracks in their  
297 damage zones than coarse-grained materials. In other words, the finer-grained materials  
298 dissipate energy more efficiently with respect to space, and therefore can develop a smaller  
299 damage zone before fracture (Brooks, 2013).
- 300 2. There seems to be an inverse correlation between the grain size and fracture toughness/tensile  
301 strength. Finer grain materials dissipate energy more efficiently in their smaller FPZ than  
302 coarse-grained materials in their larger FPZ, and thus attain higher strength properties (Brooks,  
303 2013; Nasser et al., 2005). The experiments also show that as the grain size decreases,  
304 micro-crack density increases, which means that finer-grained materials have more micro-  
305 cracks in their damage zones than coarse grained materials (Brooks, 2013). However, this is  
306 a strong statement and needs more supporting evidence.
- 307 3. Results from different experiments agree that the micro-crack density increases exponen-  
308 tially within the FPZ by approaching the fracture or fault (Scholz et al., 1993; Vermilye and

309 Scholz, 1998; Janssen et al., 2001; Backers et al., 2005; Nasser et al., 2006; Faulkner et al.,  
310 2011). Microhardness and nanoindentation experiments also confirm that the regions of in-  
311 creased micro-cracking aligns with regions of reduced nanomechanical properties (Brooks  
312 et al., 2013). This indicates the reduction of mechanical properties is due to the micro-  
313 cracking (Brooks, 2013). Micro-cracks were also found to be mainly orientated parallel to  
314 the fracture (Nasser et al., 2006).

315 4. Many experimental data show that the process zone is of a semi-elliptical (narrow-band)  
316 shape (Swanson and Spetzler, 1984; Chengyong et al., 1990; Zietlow and Labuz, 1998;  
317 Backers et al., 2005; Otsuka and Date, 2000; Wu et al., 2011; Skaråyåski et al., 2011).  
318 This structure conforms well with the assumption of cohesion-based process zone along the  
319 crack plane in the strip-yield (Dugdale-Barenblatt) model. In fact, it has been shown that the  
320 narrow-band shape of the FPZ is in a good agreement with the Dugdale-Barenblatt model  
321 (Chengyong et al., 1990; Scholz et al., 1993; Vermilye and Scholz, 1998; Nasser et al.,  
322 2006). Micro-structure analyses by Nasser et al. (2006) also show that micro-cracks in the  
323 FPZ are mainly oriented parallel to the fracture, which justify the formation of a band-shaped  
324 FPZ. From the results on sandstone, Backers et al. (2005) also observed a semi-elliptical FPZ  
325 with a length and width of about 20 mm and 10 mm. The width of the FPZ is often regarded  
326 as the characteristic length of micro-structure, and has been introduced into non-local and  
327 strain-gradient damage models to describe the width of localized zones. This often leads  
328 to capturing a deterministic size effect of quasi-brittle materials. The length seems to also  
329 depend on the rate and the significance of material softening. The arising question is in fact  
330 if there is any relation between the width and the length of the FPZ.

331 5. The FPZ size seems to be dependent on the specimen size for smaller samples. This is due to  
332 the proximity of specimen boundary to the crack tip. Experimental data on concrete suggests  
333 an increase of the FPZ length with the increase of the sample size (Otsuka and Date, 2000;  
334 Wu et al., 2011). In fact, the main sample size parameter influencing the FPZ length is the  
335 ligament size, which is the distance between the crack tip and the closest boundary. The  
336 trend shows that the FPZ length becomes smaller as the ligament size decreases. This is  
337 due to the boundary constraint in front of the crack tip, that does not allow the FPZ to fully  
338 develop. Despite the strong dependency of length on size, the width seems to hardly show  
339 any dependency on the specimen size (Otsuka and Date, 2000; Skaråyåski et al., 2011; Dong  
340 et al., 2017a).

341 6. Near the peak load, the length of the FPZ exhibits more load-dependency than its width. Ex-

342 perimental results from both AE and DIC show that the FPZ width almost stabilizes at about  
343 70 – 80% of the pre-peak load whereas its length exhibit a significant load-dependency start-  
344 ing at 80% of pre-peak and continuing over the post-peak period (Skarżyński et al., 2013;  
345 Skarżyński and Tejchman, 2013; Alam et al., 2014). This indicates that the formation of  
346 macro-cracks (micro-crack coalescence) which occurs near the peak-load does not signifi-  
347 cantly influence the width of the FPZ while it has a strong influence on the length (see results  
348 of Wu et al. (2011)). The increase of load generally causes the activation of more micro-  
349 cracks. However, it seems that near the peak load, the main energy dissipation mechanism  
350 is the coalescence of previously activated micro-cracks. Since the micro-cracks are oriented  
351 in the direction of the main crack as mentioned previously, the width is not influenced by  
352 micro-crack coalescence, while the length significantly depends on that because damage and  
353 degradation continues extending the FPZ in the direction of main crack.

- 354 7. The FPZ size identified by AE is much larger than the one obtained by microscopy (Zang  
355 and Wagner, 2000; Otsuka and Date, 2000; Janssen et al., 2001; Backers et al., 2005). This  
356 may be because there is generally a high uncertainly in locating acoustic emissions due to  
357 uncertainty in the velocity model resulted from rock anisotropy and heterogeneity. Another  
358 reason for this behaviour may be the fact that the AE is able to locate all the local failures  
359 within the body while the microscopic analyses are only surface measurements.
- 360 8. Results form AE measurements show that both tensile and shearing events are captured  
361 even when the macro-crack is subjected to pure mode I (Backers et al., 2005; Nasser et al.,  
362 2006; Alam et al., 2015). This can be explained by taking into account the fact that in  
363 essence micro-cracks are randomly oriented, and some are more susceptible to shear than  
364 tensile failure, and therefore one should not expect only tensile failure in mode I loading of  
365 original main crack. In addition, under mode I loading, the shear stress is zero only along the  
366 crack ligament, and significant shear stresses are present at other directions. These results  
367 generally suggest that both tensile and shearing failures occur in the micro-scale irrespective  
368 of the type of the loading applied on the original macro-crack.
- 369 9. Experiments on the FPZ characterization under mixed-mode loading condition show that  
370 the FPZ slightly rotate from the crack plane, and both crack opening and sliding occur at the  
371 crack mouth (Lin et al., 2014; Dong et al., 2017b).

### 372 3.4. FPZ evaluation using DIC

373 DIC is a relatively new method in experimental mechanics, whose popularity was favored by  
374 the advancements in imaging and digital image processing techniques. The DIC uses consecutive

375 imaging of the surface of a deforming body, whose surface is covered in a random speckle pattern,  
376 and calculates the surface position and displacements by correlating the patterns in space and time.  
377 Through high resolution and high speed cameras, and through the availability of robust numerical  
378 algorithms for cross correlation, the DIC is nowadays a powerful technique in experimental me-  
379 chanics, and is able to provide high resolution and precise measurements of surface displacements  
380 and strains. For this reason, DIC has been widely used recently for investigating the inception and  
381 the evolution of the strain localization in quasi-brittle materials. However, when using DIC for  
382 evaluating localized deformation in the FPZ, the calculated displacements and strains can be sen-  
383 sitive to length resolution, search patch size of images and filter size used for smoothing purposes.  
384 The following methods have been used to determine the FPZ from DIC:

- 385 • The most simple method is based on the jump of displacement across the crack plane (Corr  
386 et al., 2007; Wu et al., 2011; Lin and Labuz, 2013; Lin et al., 2014; Dong et al., 2017b,a).  
387 Based on this scheme, the distance between the two ends of the displacement jump at either  
388 sides of crack plane denotes the FPZ width, while the distance from the tip up to the point  
389 along the crack ligament at which displacement jump vanishes denotes the FPZ length. It  
390 is noteworthy that the evolution of the displacement jump by load shows three different  
391 stages: (1) Elastic phase in which no considerable jump is recognizable, (2) formation of  
392 the FPZ with moderate displacement gradient, and (3) very high gradient of displacement  
393 which occurs at the moment of instability and macro-crack initiation. The width of the FPZ  
394 shall be measured towards the end of the second phase which is expected to be near the  
395 peak load on the force-displacement curve. At any stage after this point, the opening of  
396 macro-crack surfaces known as the crack tip opening displacement has to be deduced from  
397 the distance between the two ends of the displacement jump in order to obtain a valid FPZ  
398 width. The crack mouth opening and its variation along the FPZ can also be evaluated using  
399 this method. Most of studies show a somewhat linear reduction of opening along the FPZ.
- 400 • The second method is based on strain contours and using a critical strain as a threshold to  
401 define the FPZ (Skarżyński et al., 2011; Alam et al., 2014; Enfedaque et al., 2015). Although  
402 strains are good indicators of localised zones, one needs to address the following issues when  
403 using this method: (1) How the accuracy of calculated strains in the FPZ is influenced by  
404 subset size, subset distance and filter size. (2) What value is suitable for the critical strain  
405 and which component or invariant of strain tensor shall be used.
- 406 • Skarzyński et al. (2013); Skarzyński and Tejchman (2013) discussed the objectivity of the  
407 DIC measurements at localized zones, and suggested a third method. It uses the error func-

408 tion to fit the displacement jump, and the normal distribution function to fit the strain vari-  
409 ation along a path crossing the crack plane. Their results show that the FPZ size obtained  
410 from the displacement is different from the one obtained from the strain. The average of  
411 the fitting parameters for the displacement and strain with different search patch sizes is  
412 suggested to be used to define the width of the FPZ. Their suggested method also calculates  
413 different values for the size of the FPZ when using different software.

## 414 **4. Experimental setup**

### 415 *4.1. The rock samples*

416 In order to conduct the fracture toughness and strength tests, all samples were obtained from  
417 the cores extracted from the Grimsel Test Site (GTS) in the central Swiss Alps, Switzerland, which  
418 is part of the Aare massif. The rocks found in the rock laboratory consists of granitic to gran-  
419 odioritic composition. The material originates from the borehole FBS16.003, which was drilled  
420 during the In-situ Stimulation and Circulation (ISC) experiment in this rock laboratory (Amann  
421 et al., 2018; Krietsch et al., 2018). The borehole has a length of 44 m, a diameter of 87 mm,  
422 azimuth of 219.9° and dip of 37.3°. The foliation (175/75°) in the axial plane of the core dips with  
423 approximate 11°, which makes the foliation plane almost parallel to the axis of the cores. The  
424 specimens are cut from the borehole interval 38 to 39 m for Brazilian tensile tests and 43 to 44 m  
425 for the fracture toughness tests. All the specimens were dried for 24 h at 105° C three days before  
426 testing.

427 The lithology of the tested material consists of the so-called Grimsel Granodiorite which has  
428 a magmatic fabric, which is coarse-grained, massive and slightly porphyritic (Keusen et al., 1989;  
429 Schaltegger, U., 1989; Schneeberger et al., 2017). The rock is mainly composed of phyllosilicates,  
430 feldspar and quartz, with the volumetric ratios of 28% kalifeldspar and 36% plagioclase and 36%  
431 quartz, which is close to the mineralogical transition between granodioritic and granitic compo-  
432 sition. The quartz occurs in mm sized grains, while the orthoclase shows a few mm sized grains  
433 with Carlsbad-Twins and the plagioclase occurs from a few 10 microns to mm sized grains. Bi-  
434 otite occurs as predominant phyllosilicate and defines a strong foliation. During Alpine orogeny,  
435 strong textural overprinting of the rock occurred. The maximum pressure and temperature condi-  
436 tions are of greenschist conditions with  $450^\circ \pm 30^\circ$  C and around  $6 \pm 1$  kbar pressure (Challandes  
437 et al., 2008). The plagioclase is saussuritised and mainly persists as albite and epidote. The bi-  
438 otite is partly displaced by chloride during hydrothermal fluid circulation. The planar minerals  
439 are adjusted to the Alpine foliation, such that the naming by geological terminology is a Gneiss.  
440 The presence of aligned phyllosilicates implies that grain boundaries are preferentially aligned with



441 the schistosity. The grain boundaries are initiation points for the micro-fracturing process. In the  
 442 reminder of the paper, we will associate them with pre-existing micro-cracks and refer to them  
 443 simply as micro-cracks.

444 A specific model of anisotropic elasticity is the transversely isotropic constitutive law, which is  
 445 suitable for predicting the deformational behaviour of many types of rocks including the Grimsel  
 446 Granodiorite. The transversely isotropic model defines a so-called isotropy plane, which is as-  
 447 sumed to coincide with the apparent foliation plane, and postulates that every plane transverse to  
 448 it also defines a symmetry plane. Dambly et al. (2018) investigated the orientation of the isotropy  
 449 plane in Grimsel Granodiorite and concluded that the isotropy plane coincides with the foliation  
 450 plane with a good accuracy. Hereafter, the foliation plane is used to refer to the isotropy plane in  
 451 a transversely isotropic model. Five elastic constants characterize the elasticity of the transversely  
 452 isotropic material in principal coordinates: Two Young's moduli,  $E$  and  $E'$ , are defined within  
 453 and normal to the isotropy plane, respectively; two ratios,  $\nu$  and  $\nu'$ , represent the Poisson's ratios  
 454 within and normal to the isotropy plane, respectively; and a transverse shear modulus,  $G'$ , which  
 455 defines the shear modulus in the direction transverse to the isotropy plane. Through the well-  
 456 known Saint-Venant relation, an approximation for  $G'_{sv}$  can be obtained through the other elastic  
 457 constants:  $1/G'_{sv} = 1/E + 1/E' + 2\nu'/E'$ . In reality,  $G'$  is an independent constant and can deviate  
 458 from the approximated  $G'_{sv}$ . The in-plane shear modulus,  $G$ , is dependent of  $E$  and  $\nu$  and is given  
 459 by the relation  $G = E/[2(1 + \nu)]$ . Table 2 lists the five elastic constants averaged from different  
 460 tests and measured for the Grimsel Granodiorite samples (Dambly et al., 2018; Nejati et al., 2018).

Table 2: The five elastic constants measured for Grimsel Granodiorite from uniaxial compression tests.

$E$	$E'$	$G'$	$\nu$	$\nu'$
42 GPa	21 GPa	17 GPa	0.2	0.1

#### 461 4.2. Fracture toughness and strength measurement

462 Figure 1 shows schematically the geometrical configuration of the Brazilian and SCB sam-  
 463 ples used for tensile strength and fracture toughness measurements. The isotropy plane makes  
 464 angle  $\varphi$  with the load axis in both SCB and BD tests. The geometrical details of the samples  
 465 are given in Table 3. The fracture toughness tests were conducted using four configurations  
 466  $\varphi = 0^\circ, 45^\circ, 60^\circ, 90^\circ$ , while only two configurations of  $\varphi = 0^\circ, 90^\circ$  were tested for tensile strength  
 467 measurements.

468 The prepared samples for fracture toughness were tested in a Zwick/Roell Z005 AllroundLine  
 469 uniaxial press with maximum applicable force of 5 kN and linear variable displacement trans-  
 470 ducer (LVDT). A three-point-bending fixture with central loading stamp of 10 mm diameter was

471 employed. To start the test, the specimen was preloaded with 1 N. Thereafter, the Zwick universal  
 472 testing machine was driven by a displacement criterion of 0.1 mm/min. After the load drop of  
 473 80% due to breaking, the Zwick universal testing machine stops the loading.

474 The Brazilian tensile strength specimens were tested in a Zwick/Roell 1474 RetroLine univer-  
 475 sal testing machine capable of reaching a maximum force of 100 kN. A curved loading jaw was  
 476 used to distribute the load over a portion of disk's circumference and avoid point load. To start the  
 477 test, the specimen was preloaded with 5 N. Thereafter, the Zwick universal testing machine was  
 478 driven by a displacement criterion of 0.05 mm/min. For both SCB and Brazilian disk tests, the  
 479 load and the LVDT displacement were recorded by the digital acquisition system 1 (DAS 1). Both  
 480 machines have a load resolution of 10 N and data were acquired with a rate of 100 Hz.

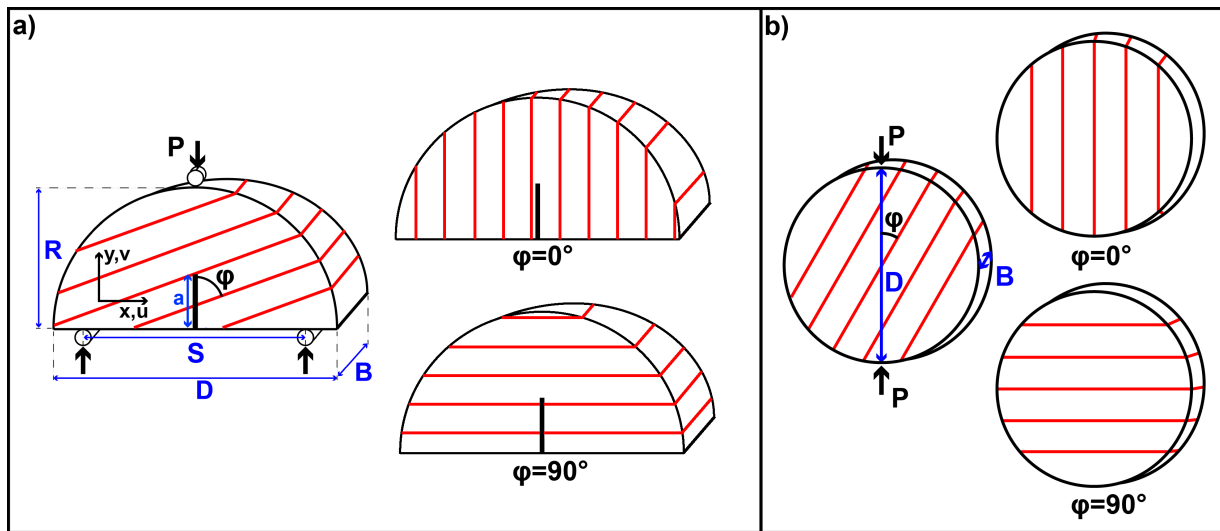


Figure 1: Schematics of (a) Semi-circular bending and (b) Brazilian disk specimens, with their two end members  $\varphi = 0^\circ, 90^\circ$  where  $\varphi$  is the angle between isotropy plane and the loading direction. A picture of the Brazilian disk with the apparent direction of isotropy plane (foliation) is also shown.

Table 3: Geometrical dimensions of specimens used for semi-circular bending (SCB) and Brazilian tensile (BD) tests.

Parameter	SCB		BD
	Values [mm]	Dimensionless values	
Diameter ( $D$ )	82.9	$B/D \approx 0.46$	83.3
Thickness ( $B$ )	37-39		37.3-40.3
Radius ( $R$ )	39.4-41.7	$S/D = 0.7$	
Span length ( $S$ )	58.4		
Crack length ( $a$ )	17-20	$\alpha = a/R = 0.41-0.5$	

### 481 4.3. Digital image correlation

482 One side of the samples were coloured white and then were sparkled by an air brush to generate  
483 a random speckle pattern. We used a VIC-3D Digital Image Correlation System, which consists  
484 of two Prosilica GT 3400 9.2 Megapixel B/ W cameras, with 80 mm focal length and capturing  
485 images with a sampling rate of 4 fps. The cameras were connected to the second digital acqui-  
486 sition system 2 (DAS 2). The two acquisition systems were synchronized by acquiring the force  
487 signal from the load cell with both the universal testing machine and the ADC converter of the  
488 DIC equipment. A reference image was recorded before deformation and a series of images was  
489 recorded during the tests. The resolution of this method depends directly on the speckle pattern on  
490 the specimen. Well-distributed and fine speckles allow to decrease bias and noise.

491 The DIC system was calibrated using a reference target reaching a calibration score (as defined  
492 in the software VIC-3D 7) of 0.018 pixels. The system setup, with the aforementioned choice  
493 of lenses, results in an average resolution of  $\tilde{40}$  pixels per millimeter. The subset size for the  
494 correlation process was chosen as a square with edge size of 35 to 47 pixels with a step size of  
495 one third of the edge size between subset centers, to deliver an average uncertainty throughout  
496 the area of interest of 0.01 pixels. This assumption was verified in the post-processing phase, and  
497 the average uncertainty for a representative test of 0.01 pixel was obtained. The DIC-system was  
498 started at the same time as the Zwick universal testing machine and stopped after total failure.

499 The series of images for each test were post-processed with VIC-3D 7 software (Correlated  
500 Solutions, Inc., 2016). The squared subset was correlated using Gaussian weight with an opti-  
501 mized 8-tap interpolation and normalized squared difference criterion. For consistency threshold,  
502 confidence margin and maximum margin was set to 0.05 pixels in the VIC-3D software. The strain  
503 calculation in VIC-3D depends on the step size and on the filter size. Smaller step sizes increase  
504 the calculation time, which is accepted. A sensitivity analysis was performed to investigate the  
505 effect of the FPZ width varying resolution edge size, search patch size and filter size at different  
506 pre-peak load. The FPZ width was compared from the  $u$ -displacement jump and the width of the  
507  $\epsilon_{xx}$ -strain field. It was found that keeping the step size at one third of the subset size and having  
508 a filter size between 5 and 9 points can reliably identify the FPZ (details given in section 6.1).  
509 Since noise level increases at such small filter sizes, an averaging scheme was used to reduce the  
510 effect of noise. MATLAB (The MathWorks Inc., 2017) was used for subsequent visualisation and  
511 further calculations.

## 5. Experimental results on toughness and strength

### 5.1. Fracture toughness anisotropy

Table 4 presents the geometrical details, the failure load as well as the calculated values of fracture toughness for 23 samples tested at different directions with respect to foliation ( $\varphi$ ). Figure 2a illustrates these data with respect to the normalized crack length, and Figure 2b shows the variation of normalized fracture toughness values against the angle  $\varphi$ . The normalization is performed with respect to the mean value of fracture toughness at the configuration  $\varphi = 90^\circ$  which corresponds to  $1.66 \text{ MPa } \sqrt{m}$ . The mean values are shown by black asterisks in Figure 2b.

Table 4: Values of the fracture toughness measured for different angles between foliation and initial crack ( $\varphi$ ).

$\varphi$	Sample ID	$\alpha$	B [mm]	$Y_I$	$P_m$ [N]	$K_{Ic}$ [MPa $\sqrt{m}$ ]	Average $K_{Ic}$
0°	FT01	0.506	39.4	5.79	1410	0.65	0.73± 0.09
	FT02	0.487	39.3	5.53	1810	0.77	
	FT05	0.417	39.1	4.78	2550	0.88	
	FT06	0.429	38.3	4.88	2200	0.82	
	FT15	0.495	39.2	5.64	1410	0.63	
	FT16	0.503	39.4	5.74	1420	0.65	
	FT21	0.412	37.3	4.73	2040	0.72	
45°	FT11	0.421	36.9	4.81	2760	1.03	0.99± 0.06
	FT12	0.415	36.7	4.76	2520	0.92	
	FT13	0.501	38.5	5.72	2100	0.97	
	FT17	0.429	37.3	4.89	2360	0.90	
	FT18	0.428	36.9	4.88	2830	1.08	
	FT25	0.514	38.1	5.89	2070	1.01	
60°	FT27	0.514	37.5	5.89	2410	1.21	1.30± 0.10
	FT28	0.484	37.6	5.50	3170	1.40	
90°	FT03	0.491	38.3	5.59	4010	1.80	1.66± 0.15
	FT04	0.495	38.3	5.64	3360	1.54	
	FT08	0.484	39.1	5.50	3510	1.50	
	FT09	0.491	36.3	5.59	4000	1.89	
	FT19	0.456	37.8	5.17	3540	1.47	
	FT20	0.427	37.6	4.87	4810	1.79	
	FT23	0.481	38.5	5.46	4020	1.72	
	FT24	0.514	38.1	5.89	3180	1.58	

The mode I fracture toughness is calculated based on the normalized stress intensity factor  $Y_I$  and the maximum load  $P_m$  as (Kuruppu et al., 2014)

$$K_{Ic} = Y_I \frac{P_m \sqrt{\pi a}}{DB} \quad (1)$$

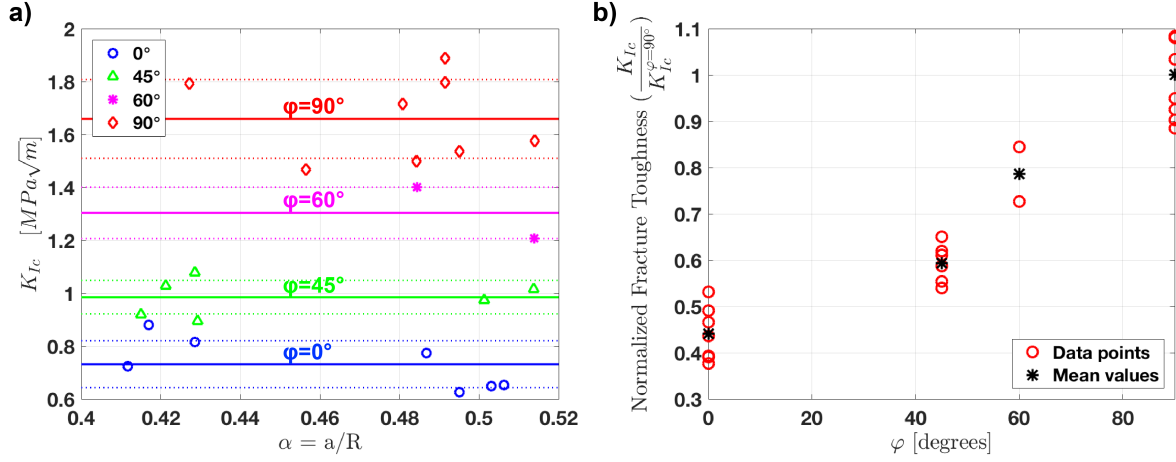


Figure 2: a) The variation of fracture toughness against the dimensionless notch ratio  $\alpha$  for different angles between the foliation and the crack orientation. The solid and dotted lines indicate mean and standard deviation (SD), respectively. b) The variation of normalized fracture toughness to the mean value at  $\varphi = 90^\circ$  against the angle between foliation and direction of initial crack  $\varphi$ .

522 where

$$Y_I = -1.297 + 9.516 \frac{S}{D} - (0.47 + 16.457 \frac{S}{D})\alpha + (1.071 + 34.401 \frac{S}{D})\alpha^2 \quad (2)$$

523 Here,  $a$  is the crack length, and  $B$  and  $D$  are the specimen thickness and diameter. The normalized  
524 stress intensity factor  $Y_I$  is a geometrical factor obtained from a fit to finite element (FE) results,  
525 and is valid only for isotropic materials (Kuruppu et al., 2014). In anisotropic cases, in addition  
526 to geometrical configuration, the material constants also influence the stress intensity factor so-  
527 lution. Several finite element analyses were performed to evaluate how strongly an anisotropic  
528 material model influences the stress intensity factor solution  $Y_I$ . The specimen was modeled  
529 and analyzed with the commercial finite element code ABAQUS. The finite element mesh and  
530 boundary condition are shown in Figure 3. An anisotropic elasticity model was used to define  
531 the transversely isotropic properties given in Table 2. The contour integral module of ABAQUS  
532 uses cylindrical domains to calculate the interaction integrals and subsequently the stress intensity  
533 factors (ABAQUS/CAE, 2014). The domain integral method to calculate the stress intensity fac-  
534 tors has been successfully used for isotropic materials (Shih and Asaro, 1988; Nejati et al., 2015),  
535 as well as anisotropic elasticity models (Wang et al., 1980; Banks-sills et al., 2005, 2007). Upon  
536 the calculation of the stress intensity factors, the normalized stress intensity factors  $Y_I$  and  $Y_{II}$  are  
537 obtained from

$$Y_I = \frac{K_I BD}{P \sqrt{\pi a}}, \quad Y_{II} = \frac{K_{II} BD}{P \sqrt{\pi a}} \quad (3)$$

538 using the geometrical and loading values employed in the finite element model. The finite element  
 539 results for isotropic as well as anisotropic material models are compared in Table 5. The values  
 540 obtained from Eq. (2) are also given for comparison. It is seen that the influence of anisotropy on  
 541 the values of the normalized stress intensity factors is minimal.

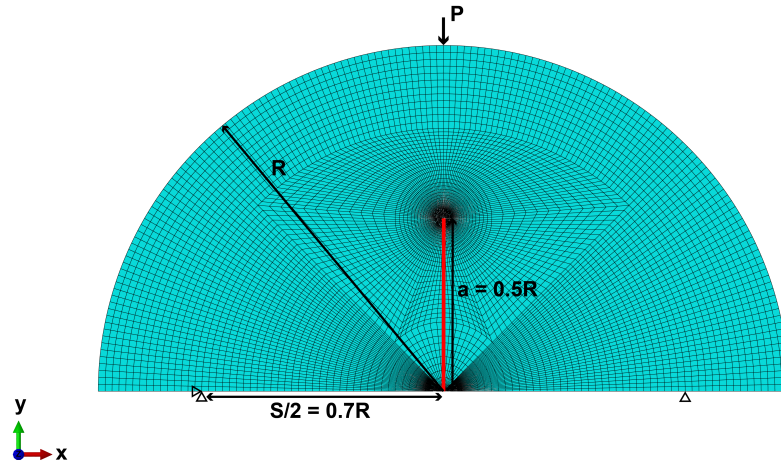


Figure 3: The finite element mesh and the boundary condition used for the finite element analyses of the SCB specimen.

Table 5: Comparison of normalized stress intensity factors obtained from isotropic and anisotropic solutions.

$\varphi$	$Y_I$			$Y_{II}$
	Eq. (2)	Isotropic (FE)	Anisotropic (FE)	Anisotropic (FE)
$0^\circ$			5.619	0
$45^\circ$	5.657	5.557	5.658	-0.640
$90^\circ$			5.527	0

542 The results indicate the following: (1)  $Y_I$  obtained from the formula given in Kuruppu et al.  
 543 (2014) overestimate the fracture toughness by only 2%. (2) The influence of the anisotropy on  
 544 the stress intensity solution  $Y_I$  is negligible. (3) Although the cases  $\varphi = 0^\circ, 90^\circ$  still induce pure  
 545 mode I using an anisotropic elasticity model, the configurations  $\varphi = 45^\circ$  yield a mixed-mode I/II  
 546 type with  $K_{II}/K_I \approx 0.1$ . This indicate that the results obtained for  $\varphi = 45^\circ, 60^\circ$  are not in fact pure  
 547 mode I fracture toughness. Note that the influence of the anisotropy on the stress intensity factor  
 548 solution can be more significant in other samples, configurations and anisotropy ratios.

549 Analyzing the fracture toughness results, the following remarks are noted:

- 550 • The values of fracture toughness are not influenced by the dimensionless notch length. It is  
 551 known that for small samples, the fracture toughness can be significantly influenced by the

552 ligament size. These results therefore seem to imply that the samples are large enough to be  
553 suitable for fracture toughness measurement of the type of rock under study.

- 554 • The ratio of the maximum fracture toughness to its minimum is 2.27, which indicates a  
555 strong anisotropy in fracture toughness. The fracture toughness is the largest for crack  
556 propagating normal to the foliation, and is the minimum when the crack grows along the  
557 foliation.
- 558 • Although the configurations  $\varphi = 0^\circ$  and  $\varphi = 90^\circ$  correspond to pure mode I crack deforma-  
559 tion, the configurations  $\varphi = 45^\circ$  and  $\varphi = 60^\circ$  involve mixed mode I/II crack growth. This is  
560 due to the elasticity anisotropy.
- 561 • Normalizing the values of the standard deviation with respect to the actual values of the frac-  
562 ture toughness gives  $0.73 \pm 12\%$ ,  $0.99 \pm 6\%$  and  $1.66 \pm 9\%$  for  $\phi = 0^\circ, 45^\circ, 90^\circ$ , respectively.  
563 The comparison of the standard deviations shows no significant variation of the scatter from  
564 one configuration to another. The reason for this small difference in scatter can be attributed  
565 to the heterogeneity and large grain size of the rock under study. Any conclusion on the  
566 difference of the scatter of the results between different configurations requires a bigger data  
567 set where the effect of heterogeneity between different configurations is minimized.

## 568 5.2. *Post-mortem fracture surface analyses*

569 Post-mortem analyses of fracture surfaces help to understand the fracturing processes in dif-  
570 ferent configurations. Such analyses may also be used to validate the accuracy of test conditions  
571 for mode I fracture toughness measurement as explained by Kuruppu et al. (2014). According  
572 to these guidelines, a deviation of more than  $0.05D$  (equivalent to 4.1 mm in our samples) of the  
573 cracked ligament from the notch plane makes the test invalid, with the resulting value being not  
574 representative of mode I fracture toughness. Figure 4 illustrates the fracture trace, both front and  
575 back views, together with the mineral analyses of fracture surfaces of all different configurations.  
576 The fracture trace is described in terms of two length parameters: maximum offset indicates the  
577 maximum distance between the fracture path and the line connecting the start and end points of the  
578 generated fracture; and kink distance is the distance between the end point of generated fracture  
579 from the loading point. The type of the minerals in the new fracture surface are also analyzed  
580 macroscopically.

581 In the case of fracture growth along foliation ( $\varphi = 0^\circ$ ), the fracture path shows very small  
582 values of kink distance (about 1 mm) and maximum offset (about 2 mm). The analysis of fracture  
583 surfaces show a high content of sheet silicates such as biotite and chlorite, indicating the fracture

584 is aligned with the biotite-rich plane. Epidote, feldspar and quartz were also observed in the  
585 new fracture surfaces, with apparent average grain size of smaller than 4 mm. When the fracture  
586 growth is normal to foliation ( $\varphi = 90^\circ$ ), the kink distance is still very low (about 2 mm), while  
587 the maximum offset (about 6 mm) is higher compared to results of  $\varphi = 0^\circ$ . The fracture seems to  
588 break through patches of stiffer quartz and feldspar rich layers, and this may be the reason why the  
589 fracture surfaces are rougher compared to the case  $\varphi = 0^\circ$ .

590 The fracture traces for  $\varphi = 45^\circ$  show much higher kink distance, about 4-6 mm, compared  
591 to the other two configurations. These values are at the border or slightly higher than the limits  
592 set based on the guideline ( $0.05D = 4.1$  mm), and therefore these test may not be considered as  
593 valid pure mode I fracture toughness tests. The maximum offset is about 4 mm which is more  
594 than  $\varphi = 0^\circ$  and less than  $\varphi = 90^\circ$ . The highly kinked fracture path may indicate the presence  
595 of mode II loading, which is in agreement with what was noted in Section 5.1. However, one  
596 should also note that the crack kinking in anisotropic rocks can be present even for pure mode  
597 I loading condition since apart from the loading, the directional-dependency of the strength can  
598 also influence the fracture growth direction (Saouma et al., 1987). The fracture traces sometimes  
599 shortly align with the foliation plane and breaks sometimes through stiffer layers containing quartz  
600 or feldspar.

601 The following remarks are noted: (1) The fracture roughness is much higher in the case of  
602  $\varphi = 90^\circ$  compared to  $\varphi = 0^\circ$ , which seems to be the influence of aligned micro-cracks along the  
603 foliation. As the angle between foliation and the initial crack,  $\varphi$ , increases, the maximum offset  
604 also raises, which is consistent with rougher fracture surfaces. (2) The largest kink distance is  
605 observed in the cases of  $\varphi = 45^\circ, 60^\circ$ . These cases show clear deviation from the original crack  
606 direction, which seems to be due to a mixed mode I/II crack loading. (3) As  $\varphi$  increases, the  
607 content of phyllosilicate minerals (e.g. biotite) on the fracture plane decreases. The fracture plane  
608 for  $\varphi = 45^\circ$  shows a higher content of feldspar and quartz compared to the one from  $\varphi = 0^\circ$  but  
609 less than  $\varphi = 90^\circ$ .

### 610 5.3. *Strength anisotropy*

611 This section presents the indirect tensile strength measurements using Brazilian disk tests. Ta-  
612 ble 6 lists the thickness, failure load and the calculated strength of six Brazilian disk specimens  
613 in two configurations  $\varphi = 0^\circ$  and  $\varphi = 90^\circ$ . In order to calculate the strength, finite element anal-  
614 yses were performed to obtain the tensile stress at the center disk using the elastic constants of  
615 transversely isotropic elasticity model given in Table 2. It is evident that the strength is strongly  
616 anisotropic, with the value in the direction normal to the foliation being 2.61 times the one along



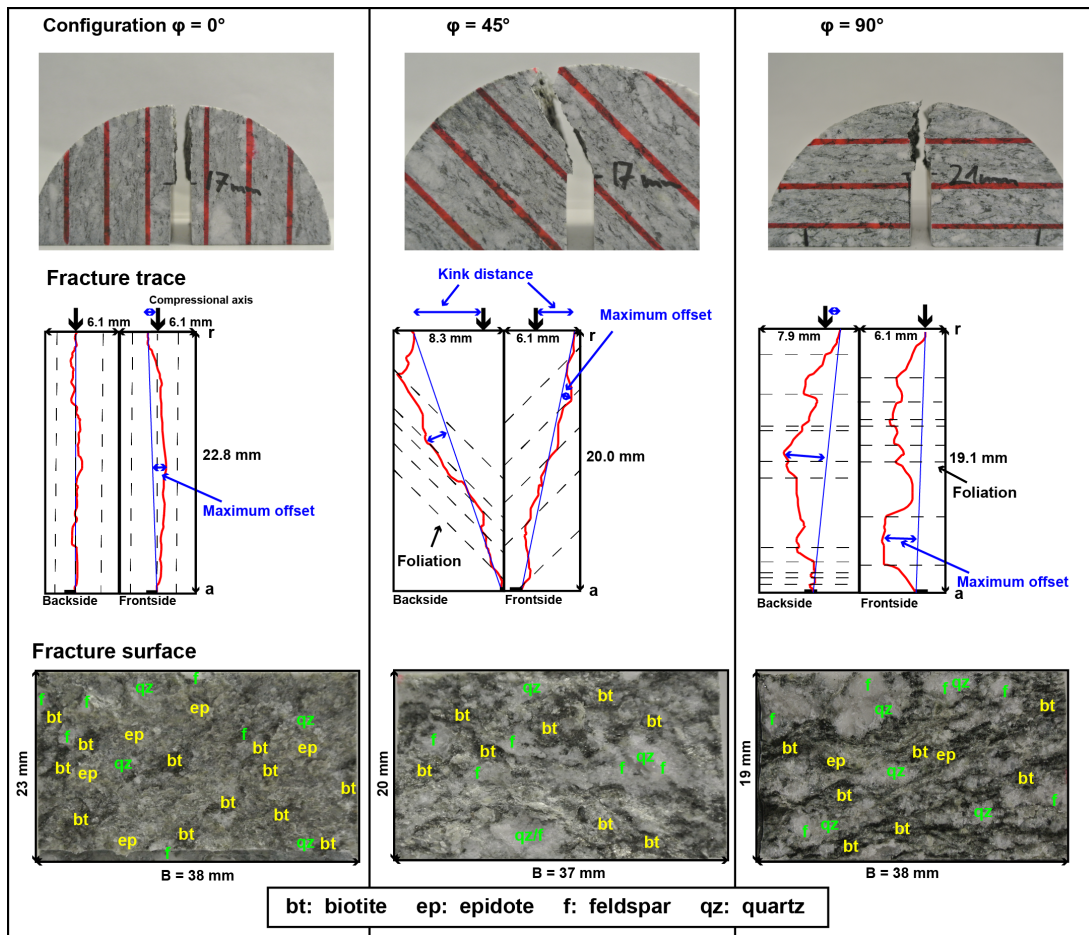


Figure 4: The visual analyses of fracture traces and surfaces for three angles between initial crack and foliation:  $\varphi = 0^\circ, 45^\circ, 90^\circ$ .

617 the foliation. This indicates the principal role of micro-cracks dominantly aligned with the folia-  
 618 tion on the strength of rock.

Table 6: The tensile strength measurements using Brazilian disk tests. The tensile stress at the center of disk was obtained using finite element solution of a transversely isotropic model based on elastic constants reported in Table 2.

$\varphi$	B [mm]	$P_m$ [kN]	$\sigma_t$ [MPa]	Average $\sigma_t$ [MPa]	Ratio
$0^\circ$	39.5	32.39	5.50	5.63±0.11	2.61
	38.6	34.3	5.68		
	40.3	36	5.71		
$90^\circ$	38.9	74.2	16.07	14.69±2.00	
	38.0	55.9	12.39		
	37.3	69.1	15.60		

619 Many previous studies have employed the isotropic solution to calculate the strength from  
620 Brazilian disk. Table 7 presents the values of strength calculated based on an isotropic elasticity  
621 behavior in comparison with the ones obtained from the finite element solution of anisotropic  
622 model. It is clear that an isotropic assumption introduces a large error, 20% in the direction of  
623 foliation and 9% in the direction normal to foliation, in the calculation of strength. In addition,  
624 an anisotropy ratio of 2.01 is obtained from isotropic model, which is significantly lower than  
625 the anisotropic prediction. It is expected that the error stemming from the isotropic solution will  
626 increase with increasing elastic anisotropy.

Table 7: Comparison of average Brazilian disk tensile strength obtained from isotropic and transversely isotropic elasticity solutions.

$\varphi$	$\sigma_t$ [MPa]	$\sigma_t^{\text{iso}}$ [MPa]	$ \sigma_t - \sigma_t^{\text{iso}} /\sigma_t$ [%]
0°	5.63	6.73	20
90°	14.69	13.33	9

627 The failure mechanism in two main directions also shows significant differences. The failure  
628 normal to the direction of foliation exhibits a more sudden and instantaneous behavior than the  
629 one along the foliation. In fact, the analyses of strains obtained from DIC measurement show the  
630 development of a band of failure along the foliation before the final rupture. This may indicate that  
631 the fracturing process is mainly due to the gradual activation of micro-cracks, which are mainly  
632 aligned with foliation, followed by their coalescence to form a macro-crack that splits the speci-  
633 men. On the other hand, when the direction of final rupture is normal to the foliation, the existing  
634 micro-cracks cannot simply connect to form the fracture, and a more complex mechanism is re-  
635 quired in the failure process perhaps including the development of new micro-cracks to connect  
636 the existing ones. Overall, the results emphasize the role of existing set of micro-cracks in the  
637 fracturing of granite, as it has also been observed in previous studies (Nasseri et al., 2005).

## 638 6. Experimental results on the FPZ

639 As discussed in the review given in Section 3, the characterization of the FPZ in quasi-brittle  
640 materials including rocks is of great importance, and is in fact a difficult task to conduct. Three  
641 suggested method to identify the FPZ from DIC results were also discussed. Due to the highly  
642 localized strain in the FPZ, the strain values should be used with caution when the FPZ is identi-  
643 fied from strain results. Also, due to the small size of the FPZ, highly accurate DIC measurements  
644 are required. Therefore, an accurate determination of the FPZ requires highly accurate DIC re-  
645 sults with appropriate smoothing methods to obtain strain in highly localized zones. This section

646 introduces an averaging method to obtain reliable values for the size of the FPZ, and discusses  
647 anisotropy of the FPZ in anisotropic rocks. The calculated values are then compared to the values  
648 estimated by models based on linear elastic fracture mechanics.

### 649 *6.1. Identification of the FPZ*

650 The DIC method provides a full-field representation of in-plane surface displacements. The  
651 spatial gradient of the displacement field is then evaluated to obtain the strain field. Due to noises  
652 involved in the displacement measurements, smoothing techniques are used to obtain the deriva-  
653 tives. The subset size is defined as a squared window used to compare two different speckle-pattern  
654 and the step size is the spacing between the subset centers. In our case the measurement needs  
655 to cover a region of 8 cm  $\times$  6 cm and the recording resolution is 3384 pixels  $\times$  2704 pixels. The  
656 average accuracy allowed is set to 0.01 pixels. During the measurements, an average resolution of  
657 40 pixels/mm was employed. The choice of the subset size between 35 to 41 pixels corresponds  
658 to 1  $\times$  1 mm<sup>2</sup>. The recommended step size is one-third of the subset size i.e. 13 pixels which is  
659 equivalent to 1/3 mm. This means that a 41  $\times$  41 pixel area is tracked at every 13 pixels. The filter  
660 size is defined as the length of the displacement values at subset centers, which smooths the strain  
661 field with increasing number of displacement points. The strain field depends directly on the step  
662 size and the filter size of the strain tensor.

663 In this paper we use an averaging window to obtain the width of the FPZ, and compare this  
664 value with the one calculated from the jump in displacement. This averaging is required since  
665 small filters are insufficient to remove sufficient noise from the strain results. This methodology  
666 is based on a window containing ten paths with intervals of 0.5 mm crossing the crack ligament  
667 near the top. Averaging the strain and displacement then removes the local noises, and facilitate  
668 observing the localized zone even with very small filter sizes. There are mainly two parameters  
669 influencing the smoothing of strain measurements: step size and filter size. The shape and the  
670 length of the FPZ is also obtained using the variation of the maximum principal strain  $\epsilon_1$  along a  
671 path ahead of the crack tip. The length is evaluated based on the distance in which the maximum  
672 principal strain is highly localized. The shape can also be determined based on the values of the  
673 maximum principal strain.

674 Figure 5 shows the variation of the FPZ width against the step and filter size at different load  
675 levels with respect to the peak (failure) load. The results in both Figures 5a and 5b are obtained  
676 from the subset size of 39 pixels to deliver an average uncertainty of displacement resolution  
677 throughout the area of interest of 0.01 pixel. In Figure 5a the filter size is kept constant at the  
678 minimum possible value (five points), while in Figure 5b, the step size of thirteen pixels is used.  
679 The displacement values are not influenced by the step size and filter size since these parameters

680 are only involved in the post-processing stage to obtain strains from displacements. These two  
681 plots suggest two main trends:

- 682 • As long as the filter size is chosen to be a small value, the calculated value for the width  
683 of localized zone is not influenced by the value of step size, and the width obtained from  
684 strains and displacement are in very good agreement. This suggest that given an appropriate  
685 choice of filter size, the step size recommended by the software (one-third of the subset size,  
686 thirteen pixels in our case) can be reliably used.
- 687 • At the constant step size, as the filter size approaches its minimum (five points), the width  
688 obtained from strain approaches the one obtained from displacement. Moreover, the cal-  
689 culated width from strain increases linearly for filter sizes above ten points. This suggests  
690 that high values of filter size increases the size of the region in which a strain smoothing  
691 procedure is applied, and therefore if the smoothing region is greater than the half of the  
692 FPZ width, the sharp displacement jump at the middle of the FPZ widens the strain profile,  
693 which leads to inaccurate measurement of the FPZ width from the strains.

694 An example to clarify the influence of the filter and step sizes is arranged as follows. Consider  
695 the width of the FPZ is 5.5 mm for the sample under study in Figure 5. A sharp gradient of  
696 displacement is expected to be present at the middle of this region due to a possible macro-crack  
697 being developed there. In this case, the distance from the sharp displacement gradient to the  
698 boundary of the FPZ is 2.75 mm. Any smoothing scheme used on a distance larger than 2.75 mm  
699 inaccurately propagates the large gradient at the center of the FPZ beyond the actual boundary  
700 of the FPZ. The choices of thirteen pixels and five points respectively for step and filter sizes  
701 results in a smoothing distance of sixty-five pixels which is equivalent to about 1.625 mm, far  
702 below 2.75 mm. However, any filter size above eight points would make the smoothing distance  
703 to extend above 2.6 mm which is almost equal to the half of the FPZ width. Figure 5b shows that  
704 the calculated width of the FPZ start to increase linearly above the filter size of about eight. This  
705 indicates that for such big filter sizes, the smoothing distance is larger than half of the FPZ, and  
706 therefore the calculated values of FPZ width are inaccurate, and the result of smoothing procedure.

707 According to this sensitivity analyses, it was concluded that a step size of thirteen pixels and  
708 filter size of five can provide accurate enough strain field for the evaluation of the FPZ size from  
709 strain localization. In fact, these parameters assure that the size of the FPZ obtained from strains  
710 are in very good agreement with the one obtained from displacement. It is noteworthy that the  
711 results in Figure 5 also show that the FPZ width is not dependent on the load level above 60%  
712 of the peak-load. This observation agrees with similar findings in previous studies (Skarzyński

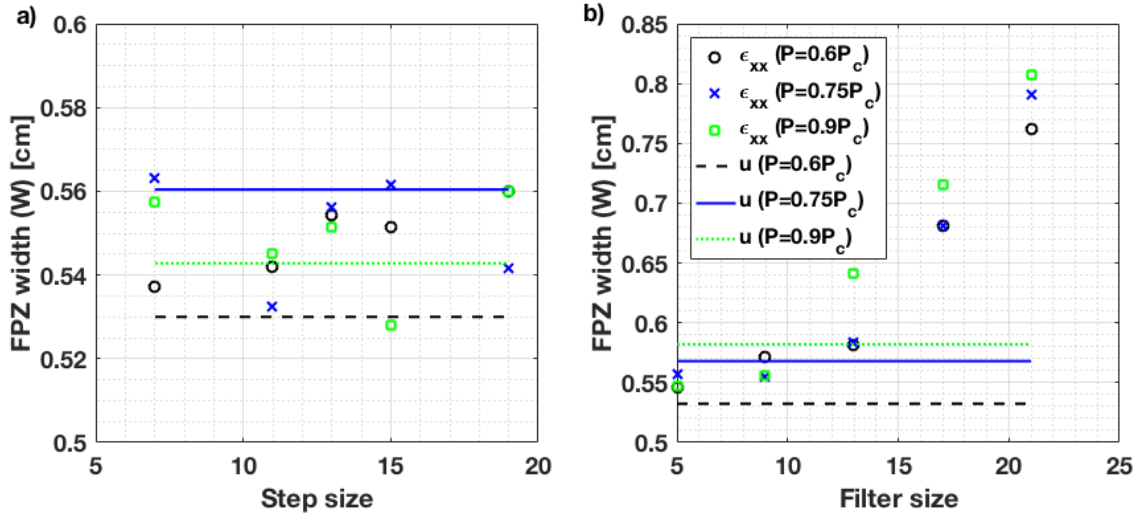


Figure 5: (a) The variation of the FPZ width obtained from localised strain  $\epsilon_{xx}$  and displacement jump  $u$  against (a) step size and (b) filter size, for three load levels of 60%, 75% and 90% of pre-peak load for a configuration  $\varphi = 0^\circ$ . The subset size for all measurements is thirty-nine pixels. In (a) and (b) the filter size and step size are five points, and thirteen pixels, respectively.

713 et al., 2013; Skarżyński and Tejchman, 2013; Alam et al., 2014; Wu et al., 2011). Note that the  
 714 variation of the FPZ width obtained from displacements and strains at different loads is small  
 715 (about 0.3 mm) compared to the actual value of the FPZ width which is about 5.5 mm.

## 716 6.2. Shape of the fracture process zone

717 Figure 6 shows the region with highly localized maximum principal strains ahead of the crack  
 718 tip in the samples tested in two configurations  $\varphi = 0^\circ, 90^\circ$ . When the crack is oriented along  
 719 foliation ( $\varphi = 0^\circ$ ), almost all samples show the development of a semi-elliptical FPZ region.  
 720 Although this is also the dominant shape in configuration  $\varphi = 90^\circ$ , the FPZ seems to show an  
 721 angular deviation from the notch plane in some samples. The angular deviation of the FPZ can be  
 722 attributed to the influence of micro-cracks oriented along the foliation, resulting in the tendency to  
 723 the change the direction of crack growth. This is the reason for having a more tortuous crack path  
 724 observed in the post-mortem analyses. The semi-elliptical FPZ shape observed in our experiments  
 725 agrees well with the results reported in many previous researches on the FPZ shape of quasi-  
 726 brittle materials (Swanson and Spetzler, 1984; Chengyong et al., 1990; Zietlow and Labuz, 1998;  
 727 Backers et al., 2005; Otsuka and Date, 2000; Wu et al., 2011; Skarżyński et al., 2011). These results

728 emphasize that butterfly-shaped FPZ obtained from analytical models are not accurate estimations  
 729 of localized zones in quasi-brittle materials.

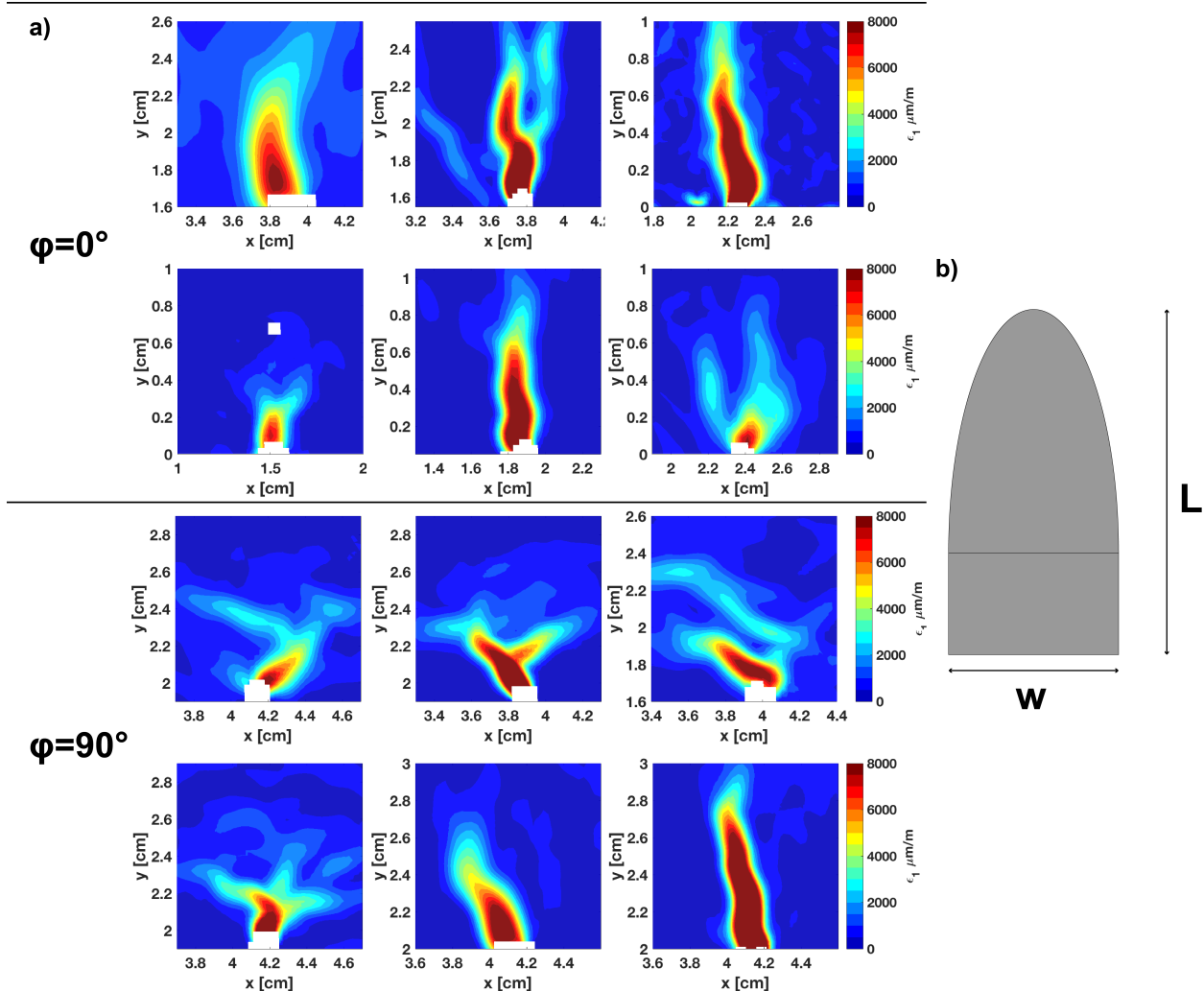


Figure 6: a) The contours of maximum principal strain showing the FPZ shape at peak load for the configurations  $\varphi = 0^\circ, 90^\circ$ . b) The FPZ is idealized schematically as a semi-elliptical region with the width of  $W$  and the length of  $L$ .

730 The overall conclusion from Figure 6 is that the FPZ seems to be developed in a semi-elliptical  
 731 region ahead of the crack tip. This finding is in very good agreement with the previous studies  
 732 and also matches the strip-yield (Dugdale-Barenblatt) model. Figure 6 shows a schematic rep-  
 733 resentation of a semi-elliptical FPZ with the width of  $W$  and the length of  $L$ . These two length  
 734 parameters seem to be independent, and are expected to be only material properties provided that  
 735 the boundary of the FPZ is fully formed (no load dependency of the FPZ boundary) and the crack

736 ligament is large enough (no boundary influence).

### 737 6.3. Size of the fracture process zone

738 Figure 7 schematically shows the identification of the FPZ width from the strain localization  
739 and displacement jump in two specimens from different configurations. These results show the  
740 agreement of the FPZ width obtained from strains and displacements. All three components of  
741 strain show localization in the process zone, with the component normal to the crack plane,  $\epsilon_{xx}$ ,  
742 being an order of magnitude greater than the other two strain components. The width of the FPZ  
743 is picked using a zone of averaging (ZOA) at 70% of pre-peak load.

744 It is noteworthy that according to the values of tensile strength and Young's moduli, a critical  
745 tensile strain of about 320 and 350 micro strains are obtained for the principal directions normal  
746 and parallel to the foliation. From the  $\epsilon_{xx}$  plots in Figure 7, it is seen that such values of critical  
747 strain are exceeded at a loading stage between 50% to 70% of the peak load. This loading level is  
748 in a very good agreement with the general belief that the development of inelastic deformation of  
749 quasi-brittle materials start at about 60-70% of the peak load (Whittaker et al., 1992).

750 Figure 8 shows the variation of maximum principal strain  $\epsilon_1$ , along twelve paths oriented at  
751 different angles with respect to the crack plane. Localization of the maximum principal strain is a  
752 good indicator of the inelastic region i.e. the FPZ. Therefore, the plots in Figure 8 can be used to  
753 define the boundary of the FPZ, whereby the length, width and shape of the FPZ are determined.  
754 At the peak load, the maximum principal strain reaches as high as 0.01 near the center of the FPZ  
755 (see Figure 8d). This high strain reduces dramatically when approaching the FPZ boundary, with  
756 localized deformation vanishing completely along the FPZ boundary. The shapes of the strains  
757 along different paths at different loads have similar trends and show an onion skin structure, where  
758 the load increases the strain in the nonlinear region, but does not influence the strain values around  
759 the FPZ. This clearly shows the localization of strain in the FPZ by increasing load. It is seen from  
760 both contours and plots that the FPZ is bigger in the configuration  $\varphi = 0^\circ$  than  $\varphi = 90^\circ$ , with the  
761 length to width ratio in both cases being  $L/W \approx 2$ .

762 Figure 8 also shows that once the boundary of the FPZ is fully formed at about 70% to 90%  
763 of the peak load, the size of the FPZ is not load dependent anymore. However, this does not mean  
764 crack extension already starts at this load level or a cohesion-less crack is developed. The activa-  
765 tion and coalescence of the micro-cracks can still continue within the FPZ, after the FPZ, or the  
766 region in which the energy dissipation occurs, has reached its ultimate size. Fakhimi et al. (2017)  
767 reported the formation of cohesion-less crack surfaces before the peak load in their experiments.  
768 However, we can not confirm such traction-free surfaces being created before the peak load in our  
769 tests. This is because (1) the DIC measurement is only surface measurement and does not give

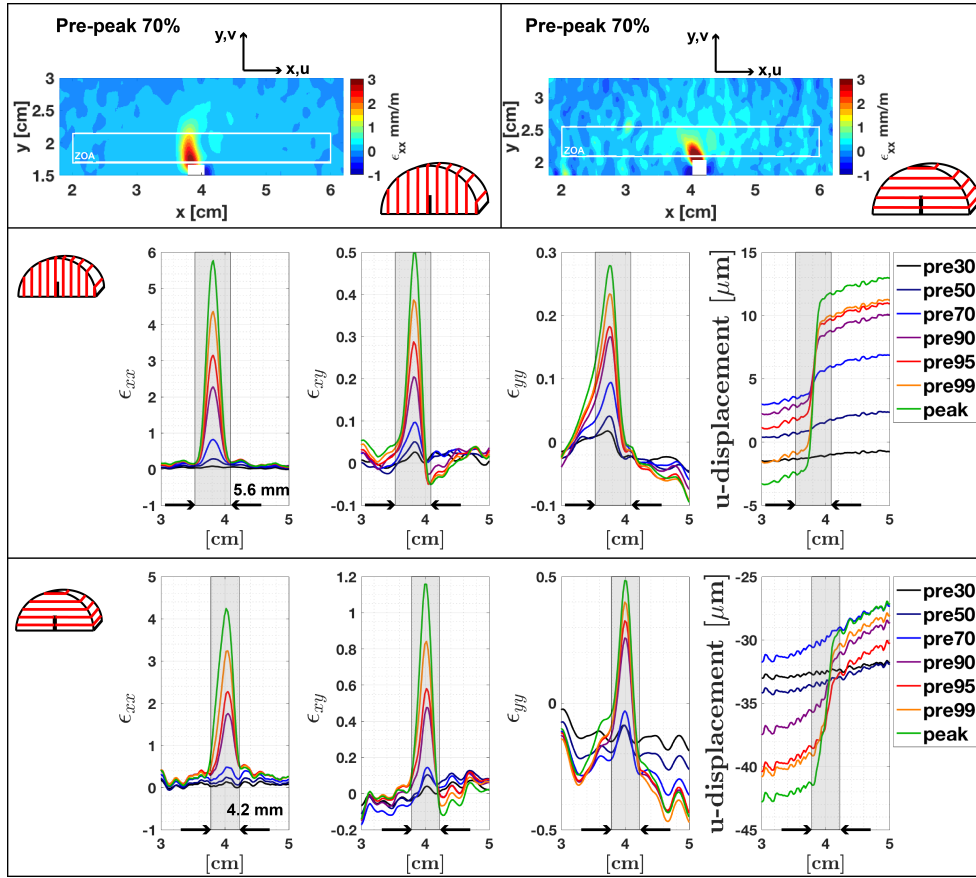


Figure 7: The calculation of the FPZ width based on localization of strain components  $\epsilon_{xx}$ ,  $\epsilon_{xy}$ ,  $\epsilon_{yy}$ , given in millistrain ( $mm/m$ ) and the jump of displacement  $u$  for two end-member configurations of  $\varphi = 0^\circ, 90^\circ$  at seven different loading stages prior to the peak load. The width of the FPZ corresponds to the width of the shaded region and measures  $w = 5.6$  mm for  $\varphi=0^\circ$  and  $w = 4.2$  mm for  $\varphi=90^\circ$ . The width of the FPZ is picked using a zone of averaging (ZOA) at 70% of pre-peak load. According to the coordinate system shown, negative values of displacement imply movements to the left.

770 any information with regard to the strains along the crack front, and (2) there is no tool to obtain  
 771 tractions within the FPZ and high values of strain do not necessarily imply a cohesion-free surface.



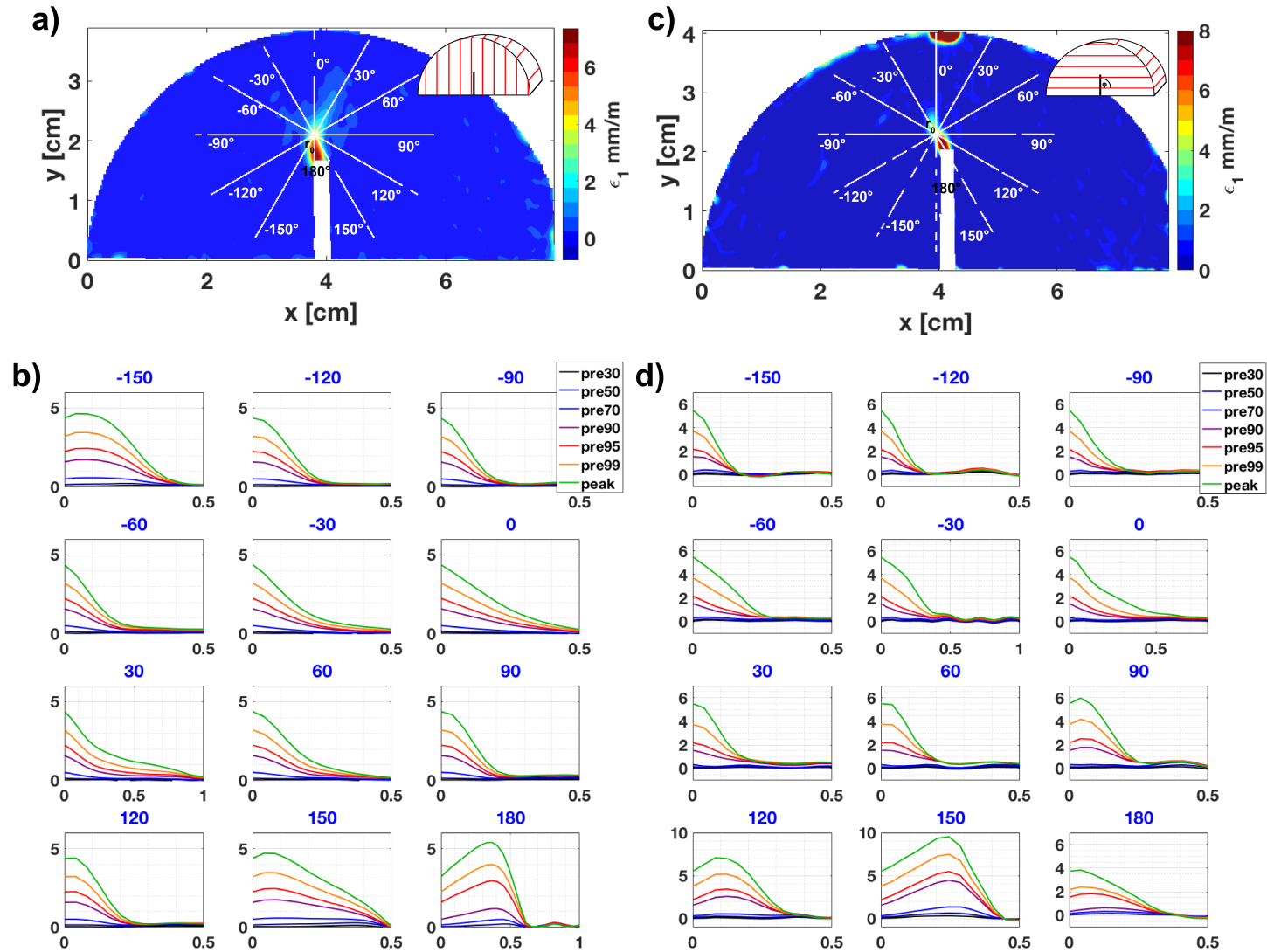


Figure 8: (a,c) The contours of maximum principal strain  $\epsilon_1$  at peak load for two configurations  $\varphi = 0^\circ, 90^\circ$ . (b,d) The variation of  $\epsilon_1$  is given in millistrain ( $mm/m$ ) along different radial paths originated from the point  $r_0$  (white lines in (a) and (c)) for different pre-peak load levels from 30% up to the peak load. The blue colored numbers in the titles of the plots in (b) and (d) indicate the specific radial path shown in (a) and (c). The unit of the  $x$ -axis in (b) and (d) is  $cm$ .

772 Figure 9 presents the measured values of the width (W) and the length (L) of the FPZ in two  
773 configurations  $\varphi = 0^\circ, 90^\circ$ . As it was previously mentioned, the boundary of the FPZ is developed  
774 earlier for  $\varphi = 0^\circ$  than  $\varphi = 90^\circ$ . The data points for  $\varphi = 90^\circ$  correspond to 90% pre-peak load,  
775 whereas the data point for  $\varphi = 0^\circ$  are at 70% of the peak load. The results for twelve samples  
776 are given in this Figure as data points, with the mean values and the standard deviation (SD)  
777 are shown by red solid lines and dotted blue lines, respectively. For crack propagating along the  
778 foliation  $\varphi = 0^\circ$ , the mean values of the six tests measure  $w = 5.4$  mm in width and  $L = 10.84$  mm  
779 in length. For the configuration  $\varphi = 90^\circ$ , the mean values for the width and the length of the FPZ  
780 are 4.7 mm and 8.8 mm, respectively. The following remarks shall be noted:

- 781 • In both configurations  $\varphi = 0^\circ$  and  $\varphi = 90^\circ$ , the average length to width ratio is  $L/W \approx 2$ .
- 782 • The fracture process zone is larger in size when the crack grows along the foliation compared  
783 to the case it propagates normal to the foliation. The ratio of the FPZ size in two directions  
784 is  $L^{\varphi=0^\circ}/L^{\varphi=90^\circ} \approx W^{\varphi=0^\circ}/W^{\varphi=90^\circ} \approx 1.2$ . This indicates that the fracture process zone is  
785 anisotropic in terms of size.
- 786 • The reason for a bigger FPZ along the foliation may be the preferred direction of micro-  
787 crack in such direction. Since the micro-cracks are oriented in the direction of crack growth,  
788 their activation and propagation can lead to a wider process zone.
- 789 • There is a negative correlation between the length and the width of the FPZ in both config-  
790 urations. Both plots show that, the higher the FPZ width, the lower the FPZ length. One  
791 can explain this trend by considering that the energy dissipated via micro-cracking is a ma-  
792 terial property which drives the resistance of the material toward crack propagation. If one  
793 assumes that this energy is constant for a configuration, any increase in the FPZ length must  
794 be accompanied with a reduction in the FPZ width.
- 795 • The scatter of the FPZ width and length data can be attributed to the heterogeneous nature  
796 of rock. The mean values of the data are therefore considered as the representative values  
797 for these parameters.

798 It is noteworthy that the full development of the FPZ in rocks is a necessary condition for a re-  
799 liable fracture toughness test. In both rocks and metals, the crack length and ligament are crucially  
800 important in order to allow the nonlinear zone to develop fully so that a representative fracture  
801 toughness can be measured. The specimen thickness requirement, however, seems to be of less  
802 importance in rock material compared to the metals. The reason is that the FPZ development in

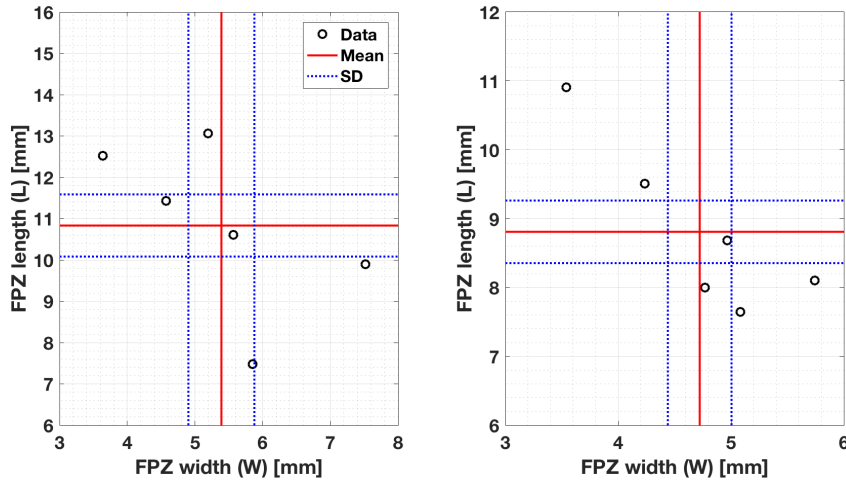


Figure 9: The measured values for the FPZ width (W) and length (L) for two cases of  $\varphi = 0^\circ$  and  $\varphi = 90^\circ$ . The mean values of the six tests are shown by red line, while the blue pointed line show the standard deviation. The results are taken from the fully formed FPZ, i.e. at 70% of pre-peak load for  $\varphi = 0^\circ$  and 90% of pre-peak load for  $\varphi = 90^\circ$ .

803 rocks is mainly due to tensile stresses, whereas the nonlinear plastic zone in metals mainly de-  
 804 velops due to shear stresses. Therefore, while the size of the plastic zone depends significantly  
 805 on the specimen thickness and out-of-plane stress, the FPZ size seems to be rather independent  
 806 of whether the plane-stress or plane-strain condition holds (Schmidt, 1980). Many experimen-  
 807 tal results obtained from different specimen types show that the measured fracture toughness is  
 808 somewhat independent of the specimen thickness (Schmidt and Lutz, 1979; Laqueche et al., 1986;  
 809 Kobayashi et al., 1986; Singh and Sun, 1990; Haberfield and Johnston, 1990; Lim et al., 1994;  
 810 Khan and Al-Shayea, 2000). Therefore, the FPZ size obtained from the surface can technically  
 811 show how the inelastic zone is developed within the solid, since a uniform FPZ is expected along  
 812 the crack front.

813 Figure 10 compares our results on the FPZ width and length with the results reported in pre-  
 814 vious research. Tarokh et al. (2017) and Otsuka and Date (2000) used concrete specimens with  
 815 aggregate sizes up to 10 mm and obtained the FPZ length and width for various sample sizes.  
 816 Backers (2004) used sandstone specimens with grain sizes between 0.1 mm and 0.5 mm. Tarokh  
 817 et al. (2017) obtained the results from DIC experiments while Backers (2004) and Otsuka and Date  
 818 (2000) conducted acoustic emission tests. This figure shows that the length to width ratio of the  
 819 FPZ mainly varies between two and four. In addition, the size of the process zone increases with  
 820 increasing the sample size, where the ratio  $L/W$  increases from two for small samples to about six  
 821 for larger ones. Overall, the results characterize the FPZ of the quasi-brittle materials as a rather

822 narrow semi-elliptical region.

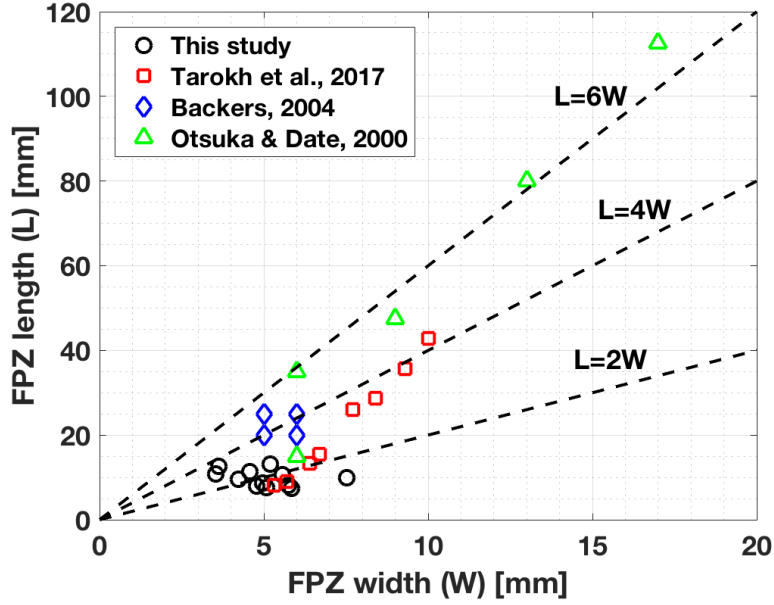


Figure 10: The comparison of the width and length of the FPZ obtained from this study with the results given in three previous studies.

## 823 7. Link between toughness, strength and the FPZ size

824 This section compares the experimental results on the FPZ size with the prediction of theo-  
 825 retical models. Let us consider a plane stress problem where one of the symmetry planes of the  
 826 material is parallel to the symmetry plane of the model (normal to  $z$ -axis). According to the gener-  
 827 alized Hooke's law, the stress-strain relationship of an elastic anisotropic material within the plane  
 828 follow

$$\begin{bmatrix} \epsilon_x \\ \epsilon_y \\ 2\epsilon_{xy} \end{bmatrix} = \begin{bmatrix} S_{11} & S_{12} & S_{16} \\ S_{21} & S_{22} & S_{26} \\ S_{61} & S_{62} & S_{66} \end{bmatrix} \begin{bmatrix} \sigma_x \\ \sigma_y \\ \tau_{xy} \end{bmatrix} \quad (4)$$

829 where  $S_{ij}$ ,  $i, j = 1, 2, 6$  are the components for the compliance matrix. Considering a crack in  
 830 the plane oriented along the  $x$ -axis, the stress field adjacent to the crack tip under mode I loading  
 831 is given by Sih et al. (1965):

$$\begin{aligned}
\sigma_x &= \frac{K_I}{\sqrt{2\pi r}} \Re \left[ \frac{\mu_1 \mu_2}{\mu_1 - \mu_2} \left( \frac{\mu_2}{\sqrt{\cos \theta + \mu_2 \sin \theta}} - \frac{\mu_1}{\sqrt{\cos \theta + \mu_1 \sin \theta}} \right) \right] \\
\sigma_y &= \frac{K_I}{\sqrt{2\pi r}} \Re \left[ \frac{1}{\mu_1 - \mu_2} \left( \frac{\mu_1}{\sqrt{\cos \theta + \mu_2 \sin \theta}} - \frac{\mu_2}{\sqrt{\cos \theta + \mu_1 \sin \theta}} \right) \right] \\
\tau_{xy} &= \frac{K_I}{\sqrt{2\pi r}} \Re \left[ \frac{\mu_1 \mu_2}{\mu_1 - \mu_2} \left( \frac{1}{\sqrt{\cos \theta + \mu_1 \sin \theta}} - \frac{1}{\sqrt{\cos \theta + \mu_2 \sin \theta}} \right) \right]
\end{aligned} \tag{5}$$

832 Here,  $r$  and  $\theta$  are the polar coordinates of the point near the tip in the crack tip local coordinate system,  $\Re$  denotes the real part of complex numbers, and  $\mu_1$  and  $\mu_2$  are the roots of the characteristic equation, and are dependent on the component of the the compliance matrix:

$$S_{11}\mu^4 - 2S_{16}\mu^3 + (2S_{12} + S_{66})\mu^2 - 2S_{26}\mu + S_{22} = 0 \tag{6}$$

835 This characteristic equation always has complex or pure imaginary roots which appear in conjugate pairs as  $\mu_1, \bar{\mu}_1$  and  $\mu_2, \bar{\mu}_2$ . Let us now consider the stress variation along the crack ligament ( $\theta = 0$ ):

$$\sigma_x = \frac{K_I}{\sqrt{2\pi r}} \Re [-\mu_1 \mu_2], \quad \sigma_y = \frac{K_I}{\sqrt{2\pi r}}, \quad \tau_{xy} = 0 \tag{7}$$

838 This equation shows the shear stress is zero along such path, and the stress component  $\sigma_y$  does not explicitly depend on the material properties. On the other hand, according to the solution by Sih et al. (1965), the stress intensity factor for a central crack in an infinite anisotropic medium with remote stress of  $\sigma$  applied normal to the crack is given by  $K_I = \sigma \sqrt{\pi a}$ . This formula is identical to the one obtained for isotropic materials, which indicates that for a central crack, the material constants of the anisotropic medium do not influence  $\sigma_y$  along the crack ligament.

844 As it was mentioned in Section 3.1, the two main models used for the estimation of the size of the inelastic zone are the Irwin approach, and the strip-yield model with uniform and linear closing stresses along the FPZ. Both models use the stress component  $\sigma_y$  along the crack ligament to obtain estimations of the inelastic zone. Since this component of stress is not influenced by the material constants according to Eq. (7), both models can be readily extended to anisotropic materials without any modification. Table 8 presents the size of the process zone obtained from these two models in comparison with the experimental results. The theoretical prediction are based on the average measurements of fracture toughness and strength given in Tables 4 and 6. It is evident from the results that the Irwin model and the strip-yield model with uniform closing stress underestimate the length of the FPZ, whereas the strip-yield model with a linear closing stress overestimate the FPZ length.

Table 8: The comparison of the FPZ length obtained from the experimental results with the theoretical models. Length values are in *mm*.

$\varphi$	Theoretical Models			Experiment
	Irwin	Strip-yield uniform traction	Strip-yield linear traction	
	$L_I = \frac{1}{\pi} \left( \frac{K_{Ic}}{\sigma_t} \right)^2$	$L_{S_u} = \frac{\pi}{8} \left( \frac{K_{Ic}}{\sigma_t} \right)^2$	$L_{S_l} = \frac{9\pi}{32} \left( \frac{K_{Ic}}{\sigma_t} \right)^2$	
$0^\circ$	5.4	6.6	14.9	10.8
$90^\circ$	4.1	5	11.3	8.8
Ratio		1.32		1.23

855 These results give an interesting insight about the type of the micro-damaging that occurs in  
856 the FPZ. Since the experimental results give values in between the predictions of the strip-yield  
857 model with uniform and linear closing (cohesion) stress distribution, it is expected the cohesion  
858 stress in reality distributes nonlinearly with higher gradient near the crack tip as shown in Figure  
859 11. This means that the gradient of the micro-damaging and reduction of strength is much higher  
860 near the tip than towards the end of the process zone. These experimental results give supporting  
861 evidence to the fact that a non-linear distribution is more realistic than uniform or linear variation  
862 of the cohesion.

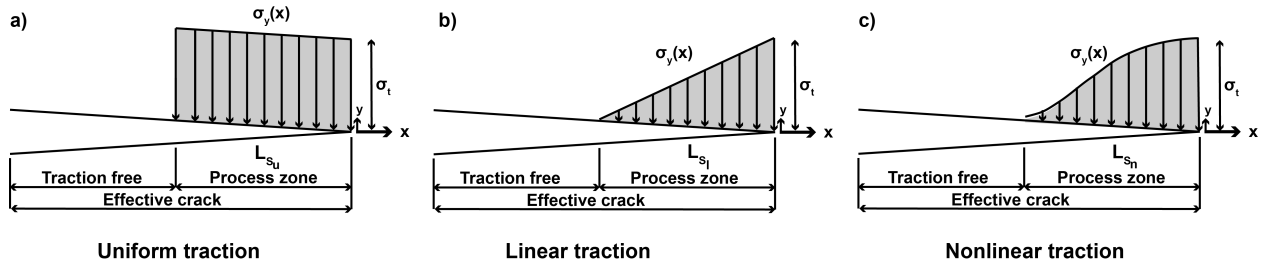


Figure 11: Schematic of models with uniform, linear and nonlinear distributions of cohesion stress along the FPZ. A cohesive model based the nonlinear distribution matches the experimental results better than the uniform and linear types.

863 Let us now compare the ratio of the process zone obtained for the principal directions. Both  
864 models predict the same ratio of the FPZ length at two configurations  $\varphi = 0^\circ$  and  $\varphi = 90^\circ$  from:

$$\frac{L^{\varphi=0^\circ}}{L^{\varphi=90^\circ}} = \left( \frac{K_{Ic}^{\varphi=0^\circ}}{K_{Ic}^{\varphi=90^\circ}} \right)^2 \times \left( \frac{\sigma_t^{\varphi=90^\circ}}{\sigma_t^{\varphi=0^\circ}} \right)^2 \quad (8)$$

865 Using the measured values of fracture toughness and strength, one can predict the ratio of the  
 866 FPZ length at two principal directions, and compares it with the experimental results of the FPZ  
 867 size:

$$\left(\frac{L^{\phi=0^\circ}}{L^{\phi=90^\circ}}\right)_{\text{Model}} = 1.32, \quad \left(\frac{L^{\phi=0^\circ}}{L^{\phi=90^\circ}}\right)_{\text{Experiment}} = 1.23 \quad (9)$$

868 Eq. (9) shows that there is a very good agreement between the results obtained directly from  
 869 the experiments, and the ones calculated from the models predicting the size of the process zone.  
 870 This gives supporting evidence that the FPZ length is in fact proportional to the square of the  
 871 fracture toughness to strength ratio:  $L \propto (K_{Ic}/\sigma_t)^2$ . The proportional constant depends on the  
 872 details of the damaging processes in the FPZ.

873 It is worth noting that the large FPZ size obtained for granodiorite samples in this study demon-  
 874 strates the development of a large nonlinear zone ahead of the crack tip. One important implica-  
 875 tion of this finding is that the LEFM concept may not be applicable to small samples since a large  
 876 portion of the sample deforms nonlinearly. The tests conducted in this research follow the size  
 877 requirements of the ISRM suggested method (Kuruppu et al., 2014):  $D \geq 2(K_{Ic}/\sigma_t)^2$ . Based on  
 878 the measured strength and fracture toughness values, the requirement for the minimum diameter  
 879 of the samples are  $D = 34$  mm for  $\phi = 0^\circ$  and  $D = 26$  mm for  $\phi = 90^\circ$ , which is significantly  
 880 lower than the diameter of the samples  $D = 82.9$  mm. The suggested size requirement assures the  
 881 full development of the FPZ in order to obtain reliable values of the fracture toughness. This raises  
 882 an important question: Is the LEFM valid for the entire range of sizes that are acceptable based on  
 883 the size requirement of the ISRM suggested method? Further research is welcome to answer this  
 884 question.

885 In addition, such big FPZ size also questions one-parameter fracture propagation criteria to be  
 886 applicable for such rocks. These criteria are formulated based on only singular terms of the crack  
 887 tip asymptotic fields, and the higher order terms are ignored based on an assumption of small pro-  
 888 cess zones. However, many experimental studies have demonstrated the significance of the higher  
 889 order terms to be included in the fracture growth criteria for rocks with large process zones (Smith  
 890 et al., 2001; Ayatollahi and Aliha, 2008; Aliha et al., 2010, 2012). Ayatollahi and Akbardoost  
 891 (2012), and Akbardoost and Ayatollahi (2014) explained the dependency of the fracture toughness  
 892 on the specimen size using a multi-parameter fracture criterion.

893 It is important to emphasize that the tensile strength results in this research are obtained indi-  
 894 rectly from the Brazilian disk test. Experimental results show that the Brazilian test overestimates  
 895 the true tensile strength, perhaps due to the applied compressive stress parallel to the loading axis  
 896 in the BD test. Nevertheless, the Brazilian tensile strength still gives reasonable estimates of the

897 true tensile strength of rock (Perras and Diederichs, 2014). We should note that the tensile strength  
898 of the rock material in the FPZ may also in essence differ from the true tensile strength of rock.  
899 This is because the rock material in the process zone is under a biaxial state of the stress and not  
900 a uniaxial one. In fact, the stress component parallel to the crack, called T-stress, is negative for  
901 the SCB specimen configuration used in this study (Ayatollahi and Aliha, 2007). Hence, the na-  
902 ture of the failures in the SCB and BD are in fact similar in the sense that a compressive stress is  
903 applied parallel to the failure plane. In this case, strength obtained from the BD test may be more  
904 representative of the failure in the FPZ rather than the true tensile strength obtained from direct  
905 tests.

## 906 **8. Conclusions**

- 907 • Experimental results of Grimsel Granodiorite samples show anisotropy ratios of 2.27 and  
908 2.61 for fracture toughness and Brazilian tensile strength, respectively. This indicates that  
909 the resistance against material failure is significantly higher in the direction normal to the  
910 foliation plane compared to the direction of the foliation plane.
- 911 • The post-mortem analyses shows significant difference of fracture path and surface charac-  
912 teristics between the two principal directions. The fracture surface shows higher roughness  
913 and more deviation from the expected path in the direction normal to the foliation compared  
914 to the direction along the foliation.
- 915 • The averaging scheme proposed for the measurement of the FPZ from DIC results calculates  
916 the width of the FPZ accurately, whereby the results from the strain and displacement fields  
917 match very well.
- 918 • The DIC results confirms the development of a semi-elliptical fracture process zone with an  
919 average length to width ratio of about two for both principal directions. These results agree  
920 well with the available results in the literature which suggest a ratio between two to four.
- 921 • The boundary of the FPZ fully forms at about 70% of the pre-peak load for crack oriented  
922 along the foliation plane, while about 90% of pre-peak load is required for crack oriented  
923 normal to the foliation. Above these load levels and before the crack extension occurs,  
924 micro-crack activation and coalescence is constrained within the boundary of the FPZ.
- 925 • Theoretical models of Irwin and strip-yield with uniform cohesion stress distribution un-  
926 derestimate the length of the FPZ. These models are based on the plastic deformation near



927 the crack tip, and one can expect they underestimate the length of the FPZ for quasi-brittle  
928 materials in which the inelastic deformation is strongly dominated by damage rather than  
929 plasticity. On the other hand, it is found the strip-yield model with a linear cohesion stress  
930 distribution overestimate the length of the process zone. The experimental results give sup-  
931 porting evidence to the fact that a nonlinear cohesion stress distribution provides a more  
932 accurate cohesive model that agrees better with the experimental results.

- 933 • The ratio of the FPZ length in two principal directions agrees very well with the theoretical  
934 predictions. This gives supporting evidence to the proportionality of the FPZ length with  
935 respect to the square of fracture toughness to tensile strength:  $L \propto (K_{Ic}/\sigma_t)^2$ , where the  
936 proportionality constant can be obtained from theoretical models or experiments.

## 937 **Acknowledgement**

938 The ISC is a project of the Deep Underground Laboratory at ETH Zurich, established by the  
939 Swiss Competence Center for Energy Research - Supply of Electricity (SCCER-SoE) with  
940 the support of the Swiss Commission for Technology and Innovation (CTI). Funding for the  
941 ISC project was provided by the ETH Foundation with grants from Shell and EWZ and by  
942 the Swiss Federal Office of Energy through a P&D grant. Nathan Dutler is supported by SNF  
943 grant no. 200021\_165677. The DIC system from the Composite Materials and Adaptive  
944 Structures laboratory was acquired through the SNF R'Equip grant no. 206021\_150729.  
945 The authors like to thank Claudio Madonna for using the Rock Deformation Laboratory and  
946 Nils Knornschild, Thomas Mörgeli and Thomas Good for their help for equipments, sample  
947 preparation and testing.

## 948 **References**

- 949 ABAQUS/CAE, 2014. Abaqus 6.14 Online Documentation. Dassault Systemes Simulia Corp., Providence, RI,  
950 USA.
- 951 Akbardoost, J., Ayatollahi, M. R., 2014. Experimental analysis of mixed mode crack propagation in brittle  
952 rocks: The effect of non-singular terms. *Engineering Fracture Mechanics* 129, 77–89.
- 953 Alam, S. Y., Loukili, A., Grondin, F., Rozière, E., 2015. Use of the digital image correlation and acoustic  
954 emission technique to study the effect of structural size on cracking of reinforced concrete. *Engineering  
955 Fracture Mechanics* 143, 17–31.
- 956 Alam, S. Y., Saliba, J., Loukili, A., 2014. Fracture examination in concrete through combined digital image  
957 correlation and acoustic emission techniques. *Construction and Building Materials* 69, 232–242.

958 Aliha, M. R., Ayatollah, M. R., Smith, D. J., Pavier, M. J., 2010. Geometry and size effects on fracture  
959 trajectory in a limestone rock under mixed mode loading. *Engineering Fracture Mechanics* 77 (11), 2200–  
960 2212.

961 Aliha, M. R., Sistaninia, M., Smith, D. J., Pavier, M. J., Ayatollahi, M. R., 2012. Geometry effects and statis-  
962 tical analysis of mode I fracture in guiting limestone. *International Journal of Rock Mechanics and Mining*  
963 *Sciences* 51, 128–135.  
964 URL <http://dx.doi.org/10.1016/j.ijrmms.2012.01.017>

965 Amann, F., Gischig, V., Evans, K., Doetsch, J., Jalali, R., Valley, B., Krietsch, H., Dutler, N., Villiger, L.,  
966 Brixel, B., Klepikova, M., Kittilä, A., Madonna, C., Wiemer, S., Saar, M. O., Loew, S., Driesner, T.,  
967 Maurer, H., Giardini, D., 2018. The seismo-hydronechanical behavior during deep geothermal reservoir  
968 stimulations: open questions tackled in a decameter-scale in situ stimulation experiment. *Solid Earth* 9 (1),  
969 115–137.

970 Anders, M. H., Laubach, S. E., Scholz, C. H., 2014. Microfractures : A review. *Journal of Structural Geology*  
971 69, 377–394.

972 ASTM, 2008. Standard Test Method for Direct Tensile Strength of Intact Rock Core Specimens. ASTM Inter-  
973 national D 3967-08.

974 Ayatollahi, M. R., Akbardoost, J., 2012. Size effects on fracture toughness of quasi-brittle materials - A new  
975 approach. *Engineering Fracture Mechanics* 92, 89–100.

976 Ayatollahi, M. R., Aliha, M. R., 2007. Wide range data for crack tip parameters in two disc-type specimens  
977 under mixed mode loading. *Computational Materials Science* 38 (4), 660–670.

978 Ayatollahi, M. R., Aliha, M. R., 2008. On the use of Brazilian disc specimen for calculating mixed mode I-II  
979 fracture toughness of rock materials. *Engineering Fracture Mechanics* 75 (16), 4631–4641.

980 Backers, T., 2004. Fracture toughness determination and micromechanics of rock under mode I and mode II  
981 loading. PhD Thesis, Geoforschungszentrum, Germany.

982 Backers, T., Stanchits, S., Dresen, G., 2005. Tensile fracture propagation and acoustic emission activity in  
983 sandstone: The effect of loading rate. *International Journal of Rock Mechanics and Mining Sciences* 42 (7-  
984 8 SPEC. ISS.), 1094–1101.

985 Banks-sills, L., Hershkovitz, I., Wawrzynek, P. A., Eliasi, R., Ingraffea, A. R., 2005. Methods for calculating  
986 stress intensity factors in anisotropic materials : Part I —  $z = 0$  is a symmetric plane. *Engineering Fracture*  
987 *Mechanics* 72, 2328–2358.

988 Banks-sills, L., Wawrzynek, P. A., Carter, B., Ingraffea, A. R., Hershkovitz, I., 2007. Methods for calculat-  
989 ing stress intensity factors in anisotropic materials : Part II — Arbitrary geometry. *Engineering Fracture*  
990 *Mechanics* 74, 1293–1307.

991 Barenblatt, G. I., 1959. The formation of equilibrium cracks during brittle fracture. General ideas and hypothe-  
992 ses. Axially-symmetric cracks. *Journal of Applied Mathematics and Mechanics* 23 (3), 622–636.

993 Barla, G., Innaurato, N., 1973. Indirect tensile testing of anisotropic rocks. *Rock Mechanics* 5 (4), 215–230.

994 Bearman, R., 1999. The use of the point load test for the rapid estimation of Mode I fracture toughness.  
995 *International Journal of Rock Mechanics and Mining Sciences* 36 (2), 257–263.

996 Bieniawski, Z., Bernede, M., 1979. Suggested methods for determining the uniaxial compressive strength and  
997 deformability of rock materials. *International Journal of Rock Mechanics and Mining Sciences & Geome-*  
998 *chanics Abstracts* 16 (2), 137–140.

- 999 Brooks, Z., 2013. Fracture Process Zone : Microstructure and Nanomechanics in Quasi-Brittle Materials. PhD  
1000 Thesis, 355.
- 1001 Brooks, Z., Ulm, F.-J., Einstein, H. H., 2012. Role of Microstructure Size in Fracture Process Zone Develop-  
1002 ment of Marble. American Rock Mechanics Association.
- 1003 Brooks, Z., Ulm, F. J., Einstein, H. H., 2013. Environmental scanning electron microscopy (ESEM) and  
1004 nanoindentation investigation of the crack tip process zone in marble. *Acta Geotechnica* 8 (3), 223–245.
- 1005 Challandes, N., Marquer, D., Villa, I. M., Sep 2008. P-t-t modelling, fluid circulation, and 39ar-40ar and rb-sr  
1006 mica ages in the aar massif shear zones (swiss alps). *Swiss Journal of Geosciences* 101 (2), 269–288.
- 1007 Chandler, M. R., Meredith, P. G., Brantut, N., Crawford, B. R., 2016. Fracture toughness anisotropy in shale.  
1008 *Journal of Geophysical Research: Solid Earth* 121, 1706–1729.
- 1009 Chandler, M. R., Meredith, P. G., Brantut, N., Crawford, B. R., 2017. Effect of temperature on the fracture  
1010 toughness of anisotropic shale and other rocks. Geological Society, London, Special Publications, SP454.6.
- 1011 Chen, C.-s., Pan, E., Amadei, B., 1998. Determination of deformability and tensile strength of anisotropic  
1012 rock using Brazilian Tests. *International journal of rock mechanics and mining sciences & geomechanics*  
1013 *abstracts* 35 (1), 43–61.
- 1014 Chengyong, W., Peidet, L., Rongshengt, H., 1990. Study of the Fracture Process Zone in Rock by Laser  
1015 Speckle Interferometry. *International Journal of Rock Mechanics & Mining Sciences & Geomechanics*  
1016 *abstracts* 27 (1), 65–69.
- 1017 Claesson, J., Bohlooli, B., 2002. Brazilian test: Stress field and tensile strength of anisotropic rocks using an  
1018 analytical solution. *International Journal of Rock Mechanics and Mining Sciences* 39 (8), 991–1004.
- 1019 Corr, D., Accardi, M., Graham-Brady, L., Shah, S., 2007. Digital image correlation analysis of interfacial  
1020 debonding properties and fracture behavior in concrete. *Engineering Fracture Mechanics* 74 (1-2), 109–  
1021 121.
- 1022 Correlated Solutions, Inc., 2016. Vic-3D Digital Imager Correlation Version 7.2.6. Irmo, Columbia, USA.
- 1023 Dai, F., Xia, K., Nasser, M. H. B., 2013. Micromechanical model for the rate dependence of the fracture  
1024 toughness anisotropy of Barre granite. *International Journal of Rock Mechanics and Mining Sciences* 63,  
1025 113–121.
- 1026 Dambly, L., Nejati, M., Vogler, D., Saar, M. O., 2018. On the direct measurement of the shear moduli in  
1027 transversely isotropic rocks using the uniaxial compression test. *International Journal of Rock Mechanics*  
1028 *and Mining Sciences*, Under Review.
- 1029 Dong, W., Wu, Z., Zhou, X., Dong, L., Kastiukas, G., 2017a. FPZ evolution of mixed mode fracture in  
1030 concrete: Experimental and numerical. *Engineering Failure Analysis* 75, 54–70.
- 1031 Dong, W., Wu, Z., Zhou, X., Wang, N., Kastiukas, G., 2017b. An experimental study on crack propagation  
1032 at rock-concrete interface using digital image correlation technique. *Engineering Fracture Mechanics* 171,  
1033 50–63.
- 1034 Dugdale, D., 1960. Yielding of steel sheets containing slits. *Journal of the Mechanics and Physics of Solids*  
1035 8 (2), 100–104.
- 1036 Dwivedi, R., Soni, A., Goel, R., Dube, A., 2000. Fracture toughness of rocks under sub-zero temperature  
1037 conditions. *International Journal of Rock Mechanics and Mining Sciences* 37 (8), 1267–1275.
- 1038 Enfedaque, A., Gálvez, J. C., Suárez, F., 2015. Analysis of fracture tests of glass fibre reinforced cement  
1039 (GRC) using digital image correlation. *Construction and Building Materials* 75, 472–487.

1040 Exadaktylos, G. E., Kaklis, K. N., 2001. Applications of an explicit solution for the transversely isotropic cir-  
1041 cular disc compressed diametrically. *International Journal of Rock Mechanics and Mining Sciences* 38 (2),  
1042 227–243.

1043 Fakhimi, A., Tarokh, A., Labuz, J. F., 2017. Cohesionless crack at peak load in a quasi-brittle material. *Engi-  
1044 neering Fracture Mechanics* 179, 272–277.

1045 Faulkner, D. R., Mitchell, T. M., Jensen, E., Cembrano, J., 2011. Scaling of fault damage zones with displace-  
1046 ment and the implications for fault growth processes. *Journal of Geophysical Research: Solid Earth* 116 (5),  
1047 1–11.

1048 Fowell, R. J., 1995. Suggested method for determining mode I fracture toughness using Cracked Chevron  
1049 Notched Brazilian Disc (CCNBD) specimens. *International Journal of Rock Mechanics and Mining Sci-  
1050 ences and* 32 (1), 57–64.

1051 Funatsu, T., Takashi, T., Kuruppu, M., 2012. Effect of Anisotropy on Fracture Toughness of Sandstone by SCB  
1052 Specimen. *ISRM Regional Symposium - 7th Asian Rock Mechanics Symposium, ISRM–ARMS7–2012–  
1053 041*.

1054 Gischig, V., Doetsch, J., Maurer, H., Krietsch, H., Amann, F., Frederick Evans, K., Nejati, M., Jalali, M.,  
1055 Valley, B., Christine Obermann, A., Wiemer, S., Giardini, D., 2018. On the link between stress field and  
1056 small-scale hydraulic fracture growth in anisotropic rock derived from microseismicity. *Solid Earth* 9 (1),  
1057 39–61.

1058 Guo, Z. K., Kobayashi, A. S., Hawkins, N. M., 1993. Further studies on fracture process zone for mode I  
1059 concrete fracture. *Engineering Fracture Mechanics* 46 (6), 1041–1049.

1060 Haberfield, C. M., Johnston, I. W., 1990. Determination of the fracture toughness of a saturated soft rock.  
1061 *Canadian Geotechnical Journal* 27, 276–284.

1062 Hoagland, R. G., Hahn, G. T., Rosenfield, A. R., 1973. Influence of microstructure on fracture propagation in  
1063 rock. *Rock Mechanics* 5 (2), 77–106.

1064 Hondros, G., 1959. The evaluation of Poisson's ratio and the modulus of materials of a low tensile resistance  
1065 by the Brazilian (indirect tensile) test with particular reference to concrete. *Aust J Appl Sci* 10 (3), 243–268.

1066 Iqbal, M. J., Mohanty, B., oct 2007. Experimental Calibration of ISRM Suggested Fracture Toughness Mea-  
1067 surement Techniques in Selected Brittle Rocks. *Rock Mechanics and Rock Engineering* 40 (5), 453–475.

1068 Irwin, G. R., 1961. Plastic zone near a crack and fracture toughness. *Sagamore Research Conference Proceed-  
1069 ings* 4, 63–78.

1070 Jalali, M., Gischig, V., Doetsch, J., Naf, R., Krietsch, H., Klepikova, M., Amann, F., Giardini, D., 2018.  
1071 Transmissivity changes and microseismicity induced by small-scale hydraulic fracturing tests in crystalline  
1072 rock. *Geophysical Research Letters* 45, 2265–2273.

1073 Janssen, C., Wagner, F., Zang, A., Dresen, G., may 2001. Fracture process zone in granite: a microstructural  
1074 analysis. *International Journal of Earth Sciences* 90 (1), 46–59.

1075 Kataoka, M., Obara, Y., 2012. Estimation of fracture toughness of anisotropic rocks by SCB test and visual-  
1076 ization of fracture by means of X-ray CT. *Test*, 667–670.

1077 Kataoka, M., Obara, Y., Kuruppu, M., 2015a. Estimation of Fracture Toughness of Anisotropic Rocks by Semi-  
1078 Circular Bend (SCB) Tests Under Water Vapor Pressure. *Rock Mechanics and Rock Engineering* 48 (4),  
1079 1353–1367.

1080 Kataoka, M., Yoshioka, S., Cho, S.-H., Soucek, K., Vavro, L., Obara, Y., 2015b. Estimation of Fracture

1081 Toughness of Sandstone by Three Testing Methods. Vietrock2015 an ISRM specialized conference (March).  
1082 Ke, C. C., Chen, C. S., Tu, C. H., 2008. Determination of fracture toughness of anisotropic rocks by boundary  
1083 element method. *Rock Mechanics and Rock Engineering* 41 (4), 509–538.  
1084 Keusen, H., Ganguin, J., Schuler, P., Buletti, M., 1989. Geologie. Tech. Rep. NTB87-14, Nagra, Wettingen.  
1085 Khan, K., Al-Shayea, N. A., 2000. Effect of Specimen Geometry and Testing Method on Mixed Mode I-  
1086 II Fracture Toughness of a Limestone Rock from Saudi Arabia. *Rock Mechanics and Rock Engineering*  
1087 33 (3), 179–206.  
1088 Khanlari, G., Rafiei, B., Abdilor, Y., 2015. Evaluation of strength anisotropy and failure modes of laminated  
1089 sandstones. *Arabian Journal of Geosciences* 8 (5), 3089–3102.  
1090 Kobayashi, R., Matsuki, K., Otsuka†, N., 1986. Size effect in the fracture toughness of Ogino tuff. *International*  
1091 *Journal of Rock Mechanics and Mining Sciences & Geomechanics Abstracts* 23 (I), 13–18.  
1092 Krietsch, H., Doetsch, J., Dutler, N. O., Jalali, M., Gischig, V. S., Loew, S., Amann, F., 2018. Comprehensive  
1093 geological data of a fractured crystalline rock mass analog for hydraulic stimulation experiments. *Nature*  
1094 *Scientific Data*. Under Review.  
1095 Krishnan, G., Zhao, X., Zaman, M., Roegiers, J.-C., 1998. Fracture toughness of a soft sandstone. *International*  
1096 *Journal of Rock Mechanics and Mining Sciences* 35 (6), 695–710.  
1097 Kuruppu, M. D., Obara, Y., Ayatollahi, M. R., Chong, K. P., Funatsu, T., 2014. ISRM-Suggested Method for  
1098 Determining the Mode I Static Fracture Toughness Using Semi-Circular Bend Specimen. *Rock Mechanics*  
1099 *and Rock Engineering* 47 (1), 267–274.  
1100 Labuz, J., Shah, S., Dowding, C., 1985. Experimental analysis of crack propagation in granite. *International*  
1101 *Journal of Rock Mechanics and Mining Sciences & Geomechanics Abstracts* 22 (2), 85–98.  
1102 Labuz, J. F., Shah, S. P., Dowding, C. H., 1987. The fracture process zone in granite: evidence and effect.  
1103 *International Journal of Rock Mechanics and Mining Sciences & Geomechanics Abstracts* 24 (4), 235–  
1104 246.  
1105 Laqueche, H., Rousseau, A., Valentin, G., 1986. Crack propagation under mode I and II loading in slate schist.  
1106 *International Journal of Rock Mechanics and Mining Sciences & Geomechanics Abstracts* 23 (5), 347–354.  
1107 Lee, H. P., Olson, J. E., Holder, J., Gale, J. F. W., Myers, R. D., 2015. The interaction of propagating opening  
1108 mode fractures with preexisting discontinuities in shale. *Journal of Geophysical Research: Solid Earth* 120,  
1109 169–181.  
1110 Lekhnitskiy, S. G., 1969. *Anisotropic Plates*. *Anisotropic Plates*, 477.  
1111 Li, D., Wong, L. N. Y., 2013. The brazilian disc test for rock mechanics applications: Review and new insights.  
1112 *Rock Mechanics and Rock Engineering* 46 (2), 269–287.  
1113 Lim, I. L., Johnston, I. W., Choi, S. K., Boland, J. N., 1994. Fracture testing of a soft rock with semi-circular  
1114 specimens under three-point bending. Part 2—mixed-mode. *International Journal of Rock Mechanics and*  
1115 *Mining Sciences & Geomechanics Abstracts* 31 (3), 185–197.  
1116 Lin, Q., Fakhimi, A., Haggerty, M., Labuz, J. F., 2009. Initiation of tensile and mixed-mode fracture in sand-  
1117 stone. *International Journal of Rock Mechanics and Mining Sciences* 46 (3), 489–497.  
1118 Lin, Q., Labuz, J. F., 2013. Fracture of sandstone characterized by digital image correlation. *International*  
1119 *Journal of Rock Mechanics and Mining Sciences* 60, 235–245.  
1120 Lin, Q., Yuan, H., Biolzi, L., Labuz, J. F., 2014. Opening and mixed mode fracture processes in a quasi-brittle  
1121 material via digital imaging. *Engineering Fracture Mechanics* 131, 176–193.

- 1122 Nasser, M. H. B., Grasselli, G., Mohanty, B., 2010. Fracture toughness and fracture roughness in anisotropic  
1123 granitic rocks. *Rock Mechanics and Rock Engineering* 43 (4), 403–415.
- 1124 Nasser, M. H. B., Mohanty, B., 2008. Fracture toughness anisotropy in granitic rocks. *International Journal*  
1125 *of Rock Mechanics and Mining Sciences* 45 (2), 167–193.
- 1126 Nasser, M. H. B., Mohanty, B., Robin, P. Y. F., 2005. Characterization of microstructures and fracture tough-  
1127 ness in five granitic rocks. *International Journal of Rock Mechanics and Mining Sciences* 42 (3), 450–460.
- 1128 Nasser, M. H. B., Mohanty, B., Young, R. P., 2006. Fracture toughness measurements and acoustic emission  
1129 activity in brittle rocks. *Pure and Applied Geophysics* 163 (5-6), 917–945.
- 1130 Nasser, M. H. B., Rezanezhad, F., Young, R. P., 2011. Analysis of fracture damage zone in anisotropic granitic  
1131 rock using 3D X-ray CT scanning techniques. *International Journal of Fracture* 168 (1), 1–13.
- 1132 Nasser, M. H. B., Tatone, B. S. A., Grasselli, G., Young, R. P., 2009. Fracture toughness and fracture rough-  
1133 ness interrelationship in thermally treated westerly granite. *Pure and Applied Geophysics* 166 (5-7), 801–  
1134 822.
- 1135 Nejati, M., Dambly, L., Saar, M. O., 2018. Measurement of elastic constants of transversely isotropic rocks  
1136 from a single uniaxial compression test. *Rock Mechanics and Rock Engineering*, Under Review.
- 1137 Nejati, M., Paluszny, A., Zimmerman, R. W., 2015. A disk-shaped domain integral method for the computation  
1138 of stress intensity factors using tetrahedral meshes. *International Journal of Solids and Structures* 69-70,  
1139 230–251.
- 1140 Olgaard, D. L., Brace, W. F., 1983. The microstructure of gouge from a mining-induced seismic shear zone.  
1141 *International Journal of Rock Mechanics and Mining Sciences* and 20 (1), 11–19.
- 1142 Otsuka, K., Date, H., 2000. Fracture Process Zone in Concrete Tension Specimen. *Engineering Fracture Me-*  
1143 *chanics* 65 (2-3), 111–131.
- 1144 Ouchterlony, F., 1988. Suggested methods for determining the fracture toughness of rock. *International Journal*  
1145 *of Rock Mechanics and Mining Sciences & Geomechanics Abstracts* 25 (2), 71–96.
- 1146 Perras, M. A., Diederichs, M. S., 2014. A Review of the Tensile Strength of Rock: Concepts and Testing.  
1147 *Geotechnical and Geological Engineering* 32 (2), 525–546.
- 1148 Saouma, V. E., Ayari, M. L., Leavell, D. A., 1987. Mixed mode crack propagation in homogeneous anisotropic  
1149 solids. *Engineering Fracture Mechanics* 27 (2), 171–184.
- 1150 Schaltegger, U., 1989. Geochemische und isotopengeochemische Untersuchungen am zentralen Aaregranit  
1151 und seinen assoziierten Gesteinen zwischen Aare und Reuss (Aaremassiv, Schweiz). Ph.D. thesis, Diss.  
1152 phil.-nat. Bern, 1989, Bern.
- 1153 Schmidt, R. A., 1980. A Microcrack Model And Its Significance to Hydraulic Fracturing And Fracture Tough-  
1154 ness Testing. The 21st U.S. Symposium on Rock mechanics (USRMS), ARMA–80–0581.
- 1155 Schmidt, R. A., Lutz, T. J., 1979. K<sub>Ic</sub> and J<sub>Ic</sub> of Westerly Granite-Effects of Thickness and In-Plane Dimen-  
1156 sions. ASTM International, 166–182.
- 1157 Schneeberger, R., de La Varga, M., Egli, D., Berger, A., Kober, F., Wellmann, F., Herwegh, M., 2017. Methods  
1158 and uncertainty estimations of 3-d structural modelling in crystalline rocks: a case study. *Solid Earth* 8 (5),  
1159 987–1002.
- 1160 Scholz, C. H., Dawers, N. H., Yu, J.-Z., Anders, M. H., Cowie, P. A., 1993. Fault growth and fault scaling  
1161 laws: Preliminary results. *Journal of Geophysical Research: Solid Earth* 98 (B12), 21951–21961.
- 1162 Shih, C. F., Asaro, R. J., 1988. Elastic-plastic analysis of cracks on bimaterial interfaces: Part I—Small scale

1163 yielding. *Journal of Applied Mechanics* 55, 299–316.

1164 Sih, G. C., Paris, P. C., Irwin, G. R., 1965. On cracks in rectilinearly anisotropic bodies. *International Journal*  
1165 *of Fracture Mechanics* 1 (3), 189–203.

1166 Singh, R. N., Sun, G., 1990. A numerical and experimental investigation for determining fracture toughness  
1167 of Welsh limestone. *Mining Science and Technology* 10, 61–70.

1168 Skaråyåski, Å., Syroka, E., Tejchman, J., 2011. Measurements and calculations of the width of the fracture  
1169 process zones on the surface of notched concrete beams. *Strain* 47, 319–332.

1170 Skarzyński, Kozicki, J., Tejchman, J., 2013. Application of DIC Technique to Concrete-Study on Objectivity  
1171 of Measured Surface Displacements. *Experimental Mechanics* 53 (9), 1545–1559.

1172 Skarzyński, L., Tejchman, J., 2013. Experimental investigations of fracture process using DIC in plain and  
1173 reinforced concrete beams under bending. *Strain* 49 (6), 521–543.

1174 Smith, D. J., Ayatollahi, M. R., Pavier, M. J., 2001. The role of T-stress in brittle fracture for linear elastic  
1175 materials under mixed-mode loading. *Fatigue and Fracture of Engineering Materials and Structures* 24 (2),  
1176 137–150.

1177 Swanson, P. L., Spetzler, H., 1984. Ultrasonic probing of the fracture process zone in rock using surface waves.  
1178 *The 25th US Symposium on Rock Mechanics (USRMS)*.

1179 Tarokh, A., Makhnenko, R. Y., Fakhimi, A., Labuz, J. F., 2017. Scaling of the fracture process zone in rock.  
1180 *International Journal of Fracture* 204 (2), 191–204.

1181 Tavallali, A., Vervoort, A., 2010. Behaviour of layered sandstone under Brazilian test conditions: Layer orien-  
1182 tation and shape effects. *International Journal of Rock Mechanics & Mining Sciences* 47, 313–322.

1183 The MathWorks Inc., 2017. Matlab version 9.3.0 (R2017b). Natick, Massachusetts, USA.

1184 Vermilye, J. M., Scholz, C. H., 1998. The process zone: A microstructural view of fault growth. *Journal of*  
1185 *Geophysical Research* 103, 12223–12237.

1186 Vervoort, A., Min, K.-b., Konietzky, H., Cho, J.-w., Debecker, B., Dinh, Q.-d., Frühwirt, T., Tavallali, A.,  
1187 2014. Failure of transversely isotropic rock under Brazilian test conditions. *International Journal of Rock*  
1188 *Mechanics and Mining Sciences* 70, 343–352.

1189 Wang, S. S., Yau, J. F., Corten, H. T., 1980. A mixed-mode crack analysis of rectilinear anisotropic solids  
1190 using conservation laws of elasticity. *International Journal of Fracture* 16 (3), 247–259.

1191 Whittaker, B. N., Singh, R. N., Sun, G., 1992. *Rock fracture mechanics: principles, design and applications*.  
1192 *Rock fracture mechanics: principles, design and applications*.

1193 Wild, K. M., Wymann, L. P., Zimmer, S., Thoeny, R., Amann, F., mar 2015. Water Retention Characteristics  
1194 and State-Dependent Mechanical and Petro-Physical Properties of a Clay Shale. *Rock Mechanics and Rock*  
1195 *Engineering* 48 (2), 427–439.

1196 Wu, Z., Rong, H., Zheng, J., Xu, F., Dong, W., 2011. An experimental investigation on the FPZ properties in  
1197 concrete using digital image correlation technique. *Engineering Fracture Mechanics* 78 (17), 2978–2990.

1198 Zang, A., Wagner, F., 2000. Fracture process zone in granite. *Journal of Geophysical Research* 105 (B10),  
1199 23651–23661.

1200 Zietlow, W. K., Labuz, J. F., 1998. Measurement of the Intrinsic Process Zone in Rock Using Acoustic Emis-  
1201 sion. *Int. J. Rock Mech. Min. Sci.* 35 (3), 291–299.